

## 50. Microactuators for Dual-Stage Servo Systems in Magnetic Disk Files

This chapter discusses the design and fabrication of electrostatic MEMS microactuators and the design of dual-stage servo systems in disk drives. It introduces fundamental requirements of disk drive servo systems, along with challenges posed by storage densities increases. It describes three potential dual-stage configurations and focuses on actuated slider assemblies using electrostatic MEMS microactuators. The authors discuss major electrostatic actuator design issues, such as linear versus rotary motion, electrostatic array configuration, and differential operation. Capacitive and piezoresistive elements may be used to sense relative slider position, while integrated gimbals and structural isolation may prove useful in improving performance. A detailed design example based on a translational, micromolded actuator illustrates several of these concepts and is accompanied by theoretical and experimental results.

The chapter continues to discuss MEMS microactuator fabrication. It describes several processes for obtaining appropriate electrostatic devices including micromolding, deep reactive-ion etching, and electroplating. The primary goal of these processes is to obtain very-high-aspect ratio structures, which improve both actuation force and structural robustness. Other fabrication issues, such as electrical interconnect formation, material selection, and processing cost, are also considered. Actuated slider fabrication is compared to that of actuated suspension and actuated head assemblies; this includes a description of an instrumented suspension, in which the suspension is instrumented with strain sensors to improve vibration detection.

The section on controller design reviews dual-stage servo control design architectures and methodologies. The considerations for controller design of MEMS microactuator dual-stage servo systems are discussed. The details of control designs using a decoupled single-input single-output (SISO) design method and the robust mixed  $H_2/H_\infty$  multivariable design method of  $\mu$ -synthesis are also presented. In the decoupled design, a self-tuning control algorithm has been developed to

compensate for the variations in the microactuator's resonance mode. In the mixed  $H_2/H_\infty$  design method, controllers can use additive or parametric uncertainties to characterize unmodeled dynamics of the VCM and variations in the microactuator's resonant mode, while providing robust performance. A comprehensive robust controller design example using multi-rate control follows. Finally, the chapter also introduces a dual-stage short-span seek control scheme based on decoupled feed-forward reference-trajectory generation.

<b>50.1 Design of the Electrostatic Microactuator</b>	<b>3</b>
50.1.1 Disk Drive Structural Requirements .....	3
50.1.2 Dual-Stage Servo Configurations ...	3
50.1.3 Electrostatic Microactuators: Comb Drives versus Parallel Plates.....	4
50.1.4 Position Sensing .....	6
50.1.5 Piezoelectric Sensing .....	8
50.1.6 Electrostatic Microactuator Designs for Disk Drives.....	9
<b>50.2 Fabrication</b> .....	<b>12</b>
50.2.1 Basic Requirements .....	12
50.2.2 Electrostatic Microactuator Fabrication Example 1.....	13
50.2.3 Electrostatic Microactuator Fabrication Example 2.....	14
50.2.4 Other Fabrication Processes .....	16
50.2.5 Suspension-Level Fabrication Processes.....	17
50.2.6 Actuated Head Fabrication .....	19
<b>50.3 Servo Control Design of MEMS Microactuator Dual-Stage Servo Systems</b> .....	<b>20</b>
50.3.1 Introduction to Disk Drive Servo Control.....	20
50.3.2 Overview of Dual-Stage Servo Control Design Methodologies.....	20
50.3.3 Servo Control and Vibration Attenuation of a MEMS Microactuator Dual-Stage Servo System with an Instrumented Suspension.....	22

<sup>15</sup>0 There were several versions available. Please make sure we worked on the correct one.

hard disk drive (HDD)  
 areal density  
 bits per inch (BPI)  
 tracks per inch (TPI)  
 voice coil motor (VCM)  
 motor!voice coil

2 Part F | Industrial Applications

50.3.4 Multi-Rate Robust Track-Following Control: A Direct Approach .....	30	50.4 Conclusions and Outlook .....	33
50.3.5 Dual-Stage Seek Control Design ....	32	References .....	34

This chapter discusses the design and fabrication of electrostatic microelectromechanical systems (MEMS) microactuators, and the design of dual-stage servo systems, in disk drives. The focus of the chapter is an actuated slider assembly using an electrostatic MEMS microactuator. We discuss major design issues, including linear versus rotary actuation, electrostatic array configuration, and integrated sensing capability. We describe several fabrication processes for obtaining the necessary devices, such as micromolding, deep reactive-ion etching, and electroplating. Dual-stage servo control design architectures and methodologies are then reviewed. We present in detail track-following controller designs based on a sensitivity-function-decoupling single-input single-output design methodology and the robust  $\mu$ -synthesis design methodology. Finally, we introduce a two-degree-of-freedom (2-DOF) short-span seek control design using a dual-stage actuator.

Since the first hard disk drive (HDD) was invented in the 1950s by IBM, disk drive storage density has been following Moore's law, doubling roughly every 18 months. The current storage density is 10 million times larger than that of the first HDD [50.1]. Historically, increases in storage density have been achieved by almost equal increases in track density, the number of tracks encircling the disk, and bit density, the number of bits in each track. However, because of limitations to superparamagnetism, future areal storage density increases in HDDs are predicted to be achieved mainly through an increase in track density [50.2].

Research in the HDD industry is now targeting an areal density of one terabit per square inch. For a predicted bit aspect ratio of 4 : 1, this translates to a linear bit density of 2 Mbits per inch (BPI) and a radial track density of 500 k tracks per inch (TPI), which in turn implies a track width of 50 nm. A simple rule of thumb for servo design in HDDs is that three times the statistical standard deviation of the position error between the head and the center of the data track should be less than 1/10 of the track width. Thus, to achieve such a storage density, nanometer-level precision of the servo system will be required.

A disk drive stores data as magnetic patterns, forming bits on one or more disks. The polarity of each bit is detected (read) or set (written) by an electromagnetic device known as the read/write head. The job of a disk drive's servo system is to position the read/write head over the bits to be read or written as they spin by on the disk. In a conventional disk drive, this is done by sweeping over the disk or disks a long arm consisting of a voice coil motor (VCM), an E-block, suspensions, and sliders, as shown in Figs. 50.1 and 50.2. A read/write head is fabricated on the edge of each slider (one for each disk surface). Each slider is supported by a suspension and flies over the surface of a disk on an air bearing. The VCM actuates the suspensions and sliders about a pivot in the center of the E-block. We describe this operation in more detail in the following section.

The key to increasing HDD servo precision is to increase the servo control bandwidth. However, the bandwidth of a traditional single-stage servo system, as shown in Fig. 50.2, is limited by the multiple mechanical resonance modes of the pivot, the E-block, and the suspension between the VCM and the head. Nonlinear friction of the pivot bearing also limits achievable servo precision. Dual-stage actuation, with a second stage actuator placed between the VCM and the head, has been proposed as a solution that would increase servo bandwidth and precision.

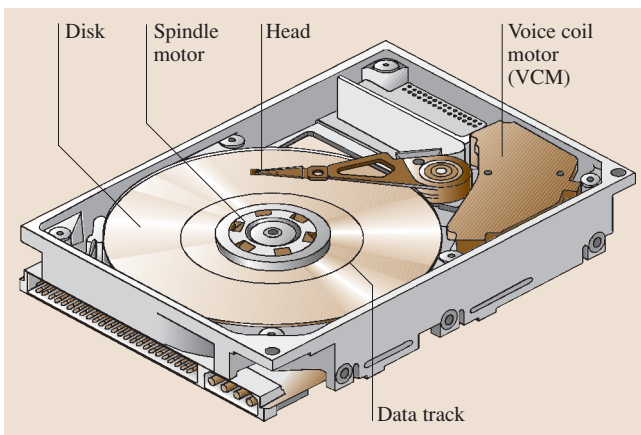


Fig. 50.1 A schematic diagram of a HDD

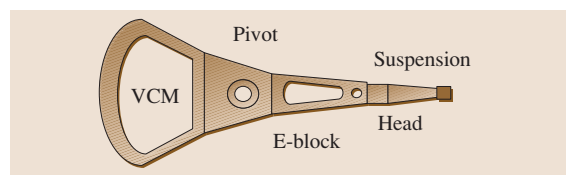


Fig. 50.2 VCM actuator in a HDD

dual-stage!configuration  
MEMS!microactuator (MA)  
electrostatic!microactuator  
mechatronic device  
slider  
dual-stage!servo system  
actuated suspension

Index entries on this page

Several different secondary actuation forces and configurations have been proposed, each having strengths and weaknesses given the requirements of HDDs. The dual-stage configurations can be categorized into three groups: actuated suspension, actuated slider, and ac-

tuated head. Within these, actuation forces include piezoelectric, electrostatic, and electromagnetic. In this chapter, we discuss design, fabrication and control of an electrostatic MEMS microactuator (MA) for actuated slider dual-stage positioning.

## 50.1 Design of the Electrostatic Microactuator

The servo system of a hard disk drive is the mechatronic device that locates and reads data on the disk. In essence, it is a large arm that sweeps across the surface of the disk. At the end of the arm is the read/write head, containing the magnetic reading and writing elements that transfer information to and from the disk.

This is accomplished using a gimbal structure. The suspension as a whole, however, should not bend or twist during the operation, as this would misdirect the head away from the track it is following.

### 50.1.1 Disk Drive Structural Requirements

The read/write head is contained in a box-like structure known as a slider. The slider has a contoured lower surface that acts as an air bearing between the head and the disk. The high-velocity airflow generated by the spinning disk pushes up on the air-bearing surface, maintaining the slider and read/write head at a constant distance from the disk, despite unevenness of the disk, permitting reliable data reading and writing.

As data densities in HDDs increase and track widths diminish, single-stage, conventional servo systems become less able to position the head precisely. Because the VCM/E-block/suspension assembly is large and massive as a unit, the speed at which the head can be controlled is limited. Furthermore, the assembly tends to have a low natural frequency, which can accentuate vibration in the disk drive and cause off-track errors. At track densities in the future approaching one terabit per square inch, the vibration induced in a disk drive by airflow alone is enough to force the head off-track.

The arm over a HDD's disk has three primary stages: the voice-coil motor (VCM), the E-block, and the suspension. In a conventional disk drive, the VCM performs all positioning of the head, swinging it back and forth across the disk. The E-block lies between the VCM and the suspension and contains the pivot point. The suspension projects from the E-block over the disk as a thin flexible structure, generally narrowing to a point at the location of the slider.

A solution to these problems is to complement the VCM with a smaller, secondary actuator to form a dual-stage servo system. The VCM continues to provide rough positioning, while the second stage actuator does fine positioning and damps out vibration and other disturbances. The smaller second-stage actuator can typically be designed to have a much higher natural frequency and be less susceptible to vibration than the VCM. Any actuator used in a dual-stage system should be inexpensive to build, require little power to operate, and preserve the stiffness properties described above that are necessary to preserve the flying height.

For a disk drive servo to operate effectively, it must maintain the read/write head at a precise height above the disk surface and within a narrow range between the disk tracks, which are arranged in concentric circles around the disk. It must also be able to seek from one track on the disk to another. Information about the track that the head is following is encoded in sectors radiating from the center of the disk, allowing the head to identify its position and distance from the center of the track. To maintain the correct flying height, the suspension must be designed with an appropriate stiffness in the vertical direction to balance an air-bearing force corresponding to the slider design in use in the drive. Meanwhile, the suspension must be flexible to roll and pitch at the slider location to permit adaptation to unevenness of the disk

### 50.1.2 Dual-Stage Servo Configurations

In the past six years, much research work has been dedicated to the exploration of suitable secondary actuators for constructing dual-stage servo systems for HDDs. These dual-stage configurations can be categorized into three groups: actuated suspension, actuated slider, and actuated head.

#### Actuated Suspension

In this approach, the suspension is redesigned to accommodate an active component, typically a piezoelectric material. This piezoelectric material stretches or flexes

#### 4 Part F | Industrial Applications

the suspension to position the slider and magnetic head. Piezoelectric material is an active actuation element that produces a large actuation force but small actuation stroke. In the actuated suspension configuration, therefore, the piezoelectric actuators are usually implemented in a leverage mechanism that can convert small actuation displacements into large head displacements. Typically this is done by placing the piezoelectric actuators away from the magnetic head (between the E-block and suspension) so that they can have a long leverage arm to gain mechanical amplification and produce a sufficient magnetic-head motion. The advantage of this approach is that the suspension can be fabricated by a conventional suspension-making process, and its dual-stage servo configuration is effective in attaining low frequency runout attenuation in the positioning servo loop. The major drawback of this approach is that the system is still susceptible to instabilities due to the excitation of suspension resonance modes. Thus, track-per-inch (TPI) servo performance can be increased but remains limited when compared to the alternative approaches. The actuated suspension approach, nonetheless is expected to be the first deployed in commercial HDDs [50.3,4].

##### Actuated Slider

In this approach, a microactuator is placed between the slider and gimbal to position the slider/magnetic heads. The resulting servo bandwidth can be higher than the previous approach because the secondary actuation bypasses the mechanical resonances of the suspension. This approach uses existing sliders and microactuators that can be batch fabricated, and thus could be cost effective. However, the size and mass of the microactuator are significant relative to those of current sliders and may interfere with the slider flying stability. Current suspensions, therefore, need to be redesigned to adopt this secondary actuator. Suitable driving forces in this approach include electrostatic, electromagnetic, and piezoelectric [50.5–8]. To further reduce the assembly task of placing the microactuator in between the gimbal structure and slider, some researchers have proposed microactuators that are either integrated with the gimbal structure [50.6] or the slider [50.9].

##### Actuated Head

In this approach, the slider is redesigned so that the microactuators can be placed inside the slider block and actuate the magnetic heads with respect to the rest of the slider body. As these microactuators are very small, they only slightly increase the slider weight and are thus capable of working with the current suspension as-

sembly. Researchers have successfully demonstrated the integrated fabrication process for fabricating the electrostatic microactuators and magnetic heads within one piece of ceramic block (slider). The embedded electrostatic microactuator has its resonance close to 30 kHz and was able to position the magnetic heads relative to the rest of the slider body by 0.5  $\mu\text{m}$  [50.10, 11]. Fully fledged integration of slider, actuator, and read/write head remains a challenge.

In this chapter, we focus on actuated slider configurations, as they involve a great deal of interesting microscale engineering. In particular, we will discuss electrostatic actuation, probably the most common method of implementing microactuation in microelectromechanical devices. Any such microactuator will exhibit certain features:

- a fixed base, which attaches to the suspension,
- a movable platform, upon which the slider rests,
- springs between the base and platform, flexible in the direction of desired motion, and stiff in all other directions, and
- an electrostatic actuation array that generates the force used to move the platform and slider.

Microactuators must also include a wiring scheme for transferring signals to and from the slider and often incorporate a structure for sensing the motion of the slider relative to the suspension. Electrostatic microactuators to be discussed in this chapter include HexSil and deep reactive-ion etching (DRIE) fabricated actuators from the University of California, Berkeley, and electroplating-formed actuators by IBM and the University of Tokyo.

Electromagnetic or piezoelectric force are alternatives to electrostatic actuation in the actuated slider configuration. Electromagnetic microactuators use ferromagnetic films to produce a force perpendicular to an applied electric field. This type of actuation potentially has low voltage requirements but requires special fabrication techniques to integrate the magnetic components into the assembly. Piezoelectric microactuators use a piezoelectric material, which expands or contracts in response to applied voltage, to move the slider. These actuators have simple fabrication, the patterning of a piece of piezoelectric material to sit between the suspension and slider, but it is difficult to obtain an adequate range of motion. A short stroke from the piezoelectric piece must be leveraged into a much larger motion at the read/write head. A piezoelectric microactuator has been produced by the TDK corporation with a 0.5  $\mu\text{m}$  stroke length at 10 V, with a 10 V bias [50.12].

### 50.1.3 Electrostatic Microactuators: Comb Drives versus Parallel Plates

Electrostatic microactuators have been studied as the secondary actuators in HDDs for their relative ease of fabrication, particularly in the actuated slider and actuated head configurations, since the structural material only needs to be conductive rather than ferromagnetic or piezoelectric. The electrostatic force is generated by applying a voltage difference between the moving shuttle and a fixed stator element. Depending on the designated motion for the shuttle, electrostatic actuators are often categorized into two groups: comb drives and parallel plates, as illustrated in Fig. 50.3.

The magnitude of the electrostatic force generated equals the rate of change of energy that is retained within the finger-like structure and varied by shuttle motion. Therefore, the electrostatic force for comb-drive actuators, in which the designated shuttle motion moves along the  $x$ -direction, as shown in Fig. 50.3, equals

$$F_{\text{comb}} = \frac{\partial E}{\partial x} = \frac{\epsilon h}{2d} V^2, \quad (50.1)$$

where  $\epsilon$  is the permittivity of air,  $x$  is the overlap between two adjacent plates,  $h$  is plate thickness, and  $d$  is the gap between two parallel plates. Similarly, the electrostatic force for parallel-plate actuators is

$$F_{\text{parallel}} = \frac{\partial E}{\partial y} = \frac{\epsilon x h}{2d^2} V^2, \quad (50.2)$$

where  $x$  is the finger overlap.

As indicated in (50.1) and (50.2), the electrostatic force for comb-drive actuators does not depend on the displacement of the moving shuttle and thus allows a long stroke while maintaining a constant electrostatic force. The electrostatic force for parallel-plate actuators, in contrast, is a nonlinear function of its shuttle motion ( $\propto 1/d^2$ ), and the maximum stroke is limited by the nominal gap between shuttle and stator. A longer stroke is achieved with a larger gap, at the expense of lower electrostatic force. For applications that require small stroke but large force output, parallel-plate actuators are preferred since the output force from parallel plates can be  $x/d$  times larger than the force from comb drives. The following equation (50.3) is easily derived from (50.1) and (50.2).

$$\frac{F_{\text{parallel}}}{F_{\text{comb}}} = \frac{x}{d}. \quad (50.3)$$

A simplified second-order differential equation is often utilized to describe the dynamic response of an

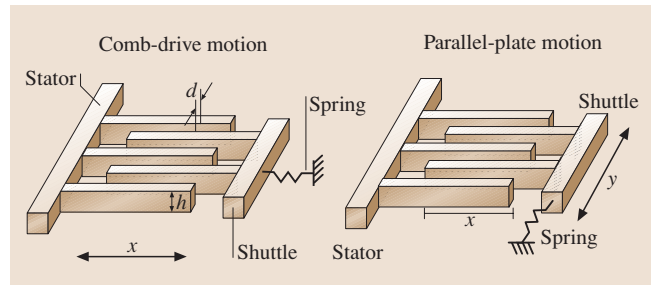


Fig. 50.3 Electrostatic microactuators: comb drives versus parallel plates

electrostatic microactuator

$$m\ddot{x}(t) + b\dot{x}(t) + K_m x(t) = F[V, x(t)], \quad (50.4)$$

where  $m$  is the mass of the moving shuttle,  $b$  is the damping coefficient of the microactuator,  $K_m$  is the spring constant of the mechanical spring that connects the moving shuttle to an anchor point, and  $F$  is the electrostatic force that can be obtained from (50.1) and (50.2).

#### Differential Drives

Because electrostatic force is always attractive, electrostatic microactuators need other features to actively control the direction of shuttle motion in servo applications, as opposed to relying on the restoring force from a mechanical spring. For this reason, the differential-drive approach, as shown in Fig. 50.4, is frequently adopted in electrostatic microactuator designs. Based on the differential-drive configuration, the simplified second-order differential equation (50.4) is rewritten as

$$m\ddot{x}(t) + b\dot{x}(t) + K_m x(t) = F[V_{\text{bias}} + V_{\text{dr}}, x_0 - x(t)] - F[V_{\text{bias}} - V_{\text{dr}}, x_0 + x(t)], \quad (50.5)$$

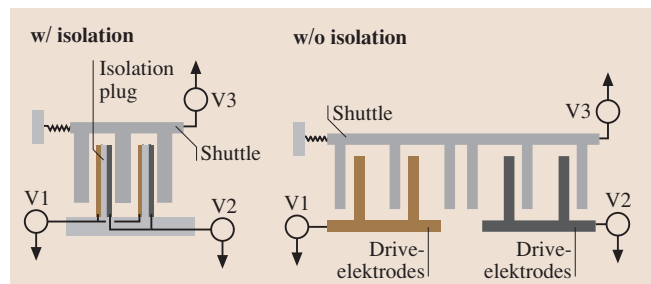


Fig. 50.4 Differential parallel-plate actuators and electrical-isolation features<sup>TS1</sup>

<sup>TS1</sup> Please check spelling of 'elektrodes'.

electrostatic!spring constant  
 voltage-to-force gain  
 spring constant  
 pull-in!instability  
 electrical!isolation  
 shuttle!finger  
 PES (photoemission spectroscopy)  
 single-input multi-output (SIMO)  
 relative position error signal (RPES)  
 multi-input multi-output (MIMO)  
 capacitive!position sensing

Index entries on this page

## 6 Part F Industrial Applications

Part F | 50.1

where  $x_0$  is the nominal position of the moving shuttle. If the differential drive is operated at the bias voltage ( $V_{\text{bias}}$ ) with a small perturbation voltage ( $V_{\text{dr}}$ ), the nonlinear force input in (50.5) can be linearized with a first-order approximation.

$$\begin{aligned}
 m\ddot{x}(t) + b\dot{x}(t) + (K_m - K_e)x(t) &= K_v V_{\text{dr}} , \\
 K_e &= 2 \frac{\partial F}{\partial x} \Big|_{V_{\text{bias}}} , \\
 K_v &= 2 \frac{\partial F}{\partial V_{\text{dr}}} \Big|_{V_{\text{bias}}} .
 \end{aligned} \tag{50.6}$$

Here  $K_e$  represents a softening electrostatic spring constant, and  $K_v$  represents the voltage-to-force gain. The electrostatic spring constant acts as a negative spring during the electrostatic microactuator operation, and its value varies with the bias voltage,  $V_{\text{bias}}$ . When the electrostatic spring constant  $K_e$  exceeds the spring constant  $K_m$  of the mechanical spring, the microactuator becomes unstable; this is often described as pull-in instability. As shown in (50.5) and (50.6), the differential configuration cancels the even-order harmonics in voltage and thus linearizes the voltage–force relation to some extent. Furthermore, in parallel-plate actuators, the differential configuration reduces the non-linearity in actuation voltage as well as in shuttle displacement.

### Electrical Isolation

Because electrostatic actuation requires multiple voltage levels for actuation force and position sensing (as discussed in the following section), electrical isolation is another challenge for designing an electrostatic microactuator. Generally speaking, when multiple voltage levels are needed in MEMS devices, electrical isolation is achieved by breaking up the parts that need to be on different voltage level and anchoring them separately to a nonconductive substrate. This approach has many drawbacks, not only because it requires a substrate in a device but also because structures have to be mechanically separated to be electrically isolated. The electrical isolation problem is far more severe in parallel-plate microactuators than comb-drive microactuators since parallel-plate actuation generally requires different voltage levels for stator fingers pulling in opposite directions.

Figure 50.4 shows an example of how an electrical-isolation feature can be utilized to increase the actuation force output in a differential parallel-plate microactuator design. As shown in the figure, without the proper electrical isolation, drive electrodes with different voltage potentials have to be placed in separate groups and result

in the same voltage difference between drive electrodes and shuttle on both sides of each shuttle finger [50.5,6]. Since electrostatic forces are always attractive, gaps on two sides of the interlaced structure cannot be made equal, otherwise the forces on two sides of a shuttle finger will be equal and the shuttle’s movement direction will be uncontrollable. With such electrical-isolation features as the isolation plug, shown on the left in Fig. 50.4, gaps in the interlaced structure can be the same width, since different voltages can be applied on the two sides of the shuttle fingers. As shown in Fig. 50.4, the design with integrated electrical-isolation features is more compact than without isolation features. Consequently, more finger structures can fit into the same amount of space, and the actuation voltage can be reduced.

### 50.1.4 Position Sensing

Most proposed HDD dual-stage servo controllers utilize only the position of the magnetic head relative to the center of data track, known in the industry as the position error signal, or PES, for closed-loop track-following control. These systems have a single-input multi-output (SIMO) control architecture. In some instances, however, it is also possible to measure the relative position error signal (RPES) of the magnetic head relative to the VCM. In this case, the control architecture is multi-input multi-output (MIMO). As shown in [50.13], RPES can be used in a MIMO controller to damp out the second-stage actuator’s resonance mode and enhance the overall robustness of the servo system.

Capacitive position sensing and piezoresistive position sensing are two popular sensing mechanisms among electrostatic microactuator designs. Each of these sensing mechanisms is discussed in more detail in the following sections.

#### Capacitive Position Sensing

Capacitive position sensing is based on shuttle movement causing a capacitance change between the moving shuttle and fixed stators. By measuring the change in capacitance, it is possible to determine the shuttle location relative to the fixed stator. The output voltage ( $V_o$ ) for both differential drives in Fig. 50.5 equals  $2\delta C/C_i V_s$ . The capacitance change due to shuttle movement ( $dC/dx$ ) can be derived and the output voltage ( $V_o$ ) for the comb drives and parallel plates can be formulated as a function of shuttle displacement.

$$V_{\text{comb}} = 2 \frac{C_s}{C_i} \frac{\delta x}{x_0} V_s ,$$

shuttle!displacement  
 parallel-plate!sensing  
 position!sensing resolution  
 1/f noise  
 noise!1/f  
 feedback!loop

Index entries on this page

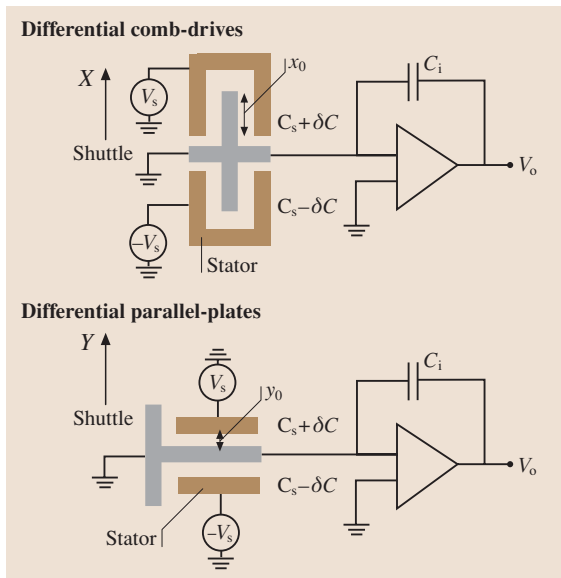


**Fig. 50.5** Capacitive position sensing. Comb-drive versus parallel-plate motion

$$V_{\text{parallel}} = 2 \frac{C_s}{C_i} \frac{y_0 \delta y}{y_0^2 - \delta y^2} V_s, \quad (50.7)$$

$$\approx 2 \frac{C_s}{C_i} \frac{\delta y}{y_0} V_s,$$

where  $x_0$  is the nominal overlap for interlaced fingers and  $y_0$  is the nominal gap between overlapped fingers, as shown in Fig. 50.5.

As indicated by (50.7), the voltage output for the comb-drive sensing structure,  $V_{\text{comb}}$ , is linear with shuttle displacement. On the other hand, the sensing configuration that makes use of the parallel-plate motion has better sensitivity for detecting shuttle motion since  $y_0$  is usually smaller than  $x_0$ . Although the nonlinearity in parallel-plate sensing can be linearized by the differential drive configuration to some extent, in a design example of a  $4 \mu\text{m}$  gap with a  $1 \mu\text{m}$  stroke, the linear model shown in (50.7) still produces 6% deviation from the nonlinear model.

Among electrostatic microactuators that use capacitive position sensing, the capacitance variation due to shuttle motion ( $dC/dx$ ) is typically at the level of  $100 \text{ fF}/\mu\text{m}$ . In order to obtain  $10 \text{ nm}$  position sensing resolution, the capacitance-sensing circuit must be able to detect capacitance variation of  $1 \text{ fF}$  in the presence of parasitic capacitance and offset/mismatches from op-amps, which can easily result in an output voltage orders of magnitude larger than the output voltage from

the designated capacitance variation. In most capacitive position sensing, the limiting factor for the sensing resolution is not the thermal noise but the sensing circuit's design.

Here we introduce two basic capacitance-sensing circuits suitable for high-resolution position sensing [50.14]. The concept of the synchronous scheme, as shown in Fig. 50.6 I, is to reduce the impedance of sense capacitors as well as the offset and  $1/f$  noise from op-amps by applying modulation techniques to the sense voltage ( $V_s$ ). The  $R_{\text{dc}}$  resistor on the feedback loop sets the DC voltage level at the input nodes of the charge integrator. The effect of the presence of parasitic capacitance ( $C_p$ ) is nullified by the virtual ground condition from the op-amps. The major drawback of the synchronous scheme is that the DC-setting resistor ( $R_{\text{dc}}$ ) has to be large to ensure the proper gain for the capacitance sensing [50.14], which introduces excessive thermal noise into the sensing circuit. In addition, a large resistor usually consumes a large die space in implementation.

A switched-capacitance scheme, as shown in Fig. 50.6 II, is one alternative that avoids the use of the

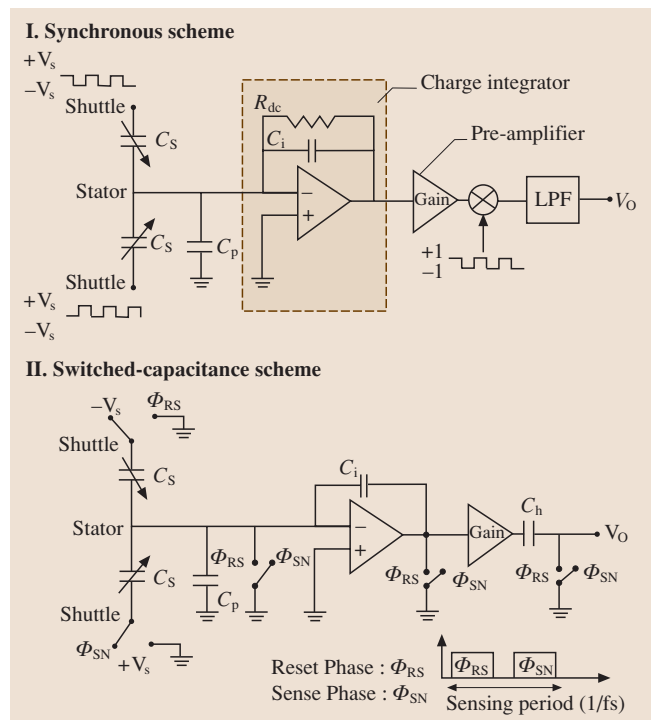


**Fig. 50.6** Capacitive position-sensing circuits. The synchronous scheme versus the switched-capacitance scheme

Part F | 50.1

DC-setting resistor. The capacitance-sensing period is broken into two phases: the reset phase and sense phase. During the reset phase, the input/output nodes of the capacitors and the input voltage to op-amps are set to the ground or reference level to ensure proper DC voltage for the charge integrator. During the sense phase, the sense voltage  $\pm V_s$  is applied to the sense capacitors, and the amount of charge proportional to the mismatch in the sense capacitors is integrated on the capacitor  $C_i$ , thus producing an output voltage proportional to the capacitance mismatch from the sense capacitors. This approach replaces the large DC-setting resistor by capacitors and switches and results in a much smaller die compared to the synchronous scheme. Furthermore, the switching technique allows more design flexibility for system integration and performance improvement because of the ability to allocate separate phases for various operations. The major drawback of this design is that it draws noise into the sensing circuits from switches and the sampling capacitor  $C_h$ . However, these noises can be compensated by dividing the sense phase into  $2 \approx 3$  sub-sense phases [50.14], at the expense of a complicated circuit design.

#### Piezoresistive Sensing

Piezoresistive films have been widely used as strain-sensitive components in a variety of MEMS devices, including pressure sensors and vibration sensors. Generally speaking, piezoresistive sensing techniques require less-complicated sensing circuits and perform better in a severe environment than other sensing techniques. When a piezoresistive film is subjected to stress, the film resistivity and dimensions change. The fractional change of resistance is proportional to the deformation of the piezoresistive film. For a small change of resistance, this relation can be expressed as,

$$\frac{\Delta R}{R} = K \cdot \epsilon, \quad (50.8)$$

where  $R$  is the resistance of the piezoresistive film,  $K$  is its gage factor and  $\epsilon$  is the strain. In microactuator designs, the piezoresistive film is usually applied to the spring structure that connects the moving shuttle to an anchor point. When the shuttle moves, it stretches the spring as well as the piezoresistive film; consequently, the piezoresistive film produces a deformation signal proportional to the shuttle displacements. As a result, piezoresistive sensing is easier to implement than capacitive position sensing, but the sensing resolution is usually lower due to the larger thermal noise introduced by the resistance of the piezoresistive film.

Another application of piezoresistive sensing, aside from measuring relative slider position, is to detect vibration in the suspension itself. The idea is to sense airflow-induced vibration of the suspension and feed that information forward to an actuated slider to damp out motion at the head. Piezoresistors used for this purpose can be made from metal or semiconductor materials, arranged as a strip or series of strips oriented along the direction of vibration strain. It is important that these sensors observe all vibration modes that contribute to off-track error, so a number of optimization schemes for locating the sensors have been developed [50.15]. One method is to maximize the minimum eigenvalue of the observability matrix of the sensor or sensors. This ensures that all relevant modes are observed. Another method is to minimize a linear quadratic Gaussian control problem over potential sensor locations [50.16]. This serves to determine an optimal placement from the perspective of a linear controller.

#### 50.1.5 Piezoelectric Sensing

Piezoelectric materials are also widely used to build sensors such as surface-acoustic-wave devices, pressure sensors and accelerometers. Devices fabricated from piezoelectric materials are energy convertors that convert mechanical to electrical energy and vice versa. Depending on how the devices are used, they can be utilized as sensors or as actuators. When acting as sensors, the external stress causes electrical asymmetry inside the material structure. As a consequence, charges are generated to compensate the asymmetry. The amount of generated charge depends both on the applied force and the crystal structure of the material. This phenomenon, called the direct piezoelectric effect, is usually expressed in an orthogonal coordinate system as

$$D_i = d_{ij}T_j + \epsilon_{ik}^T E_k, \quad (50.9)$$

where  $D_i$ ,  $d_{ij}$ ,  $T_j$ ,  $\epsilon_{ik}^T$  and  $E_k$  are the electric displacement, piezoelectric constant, stress, dielectric constant and electric field, respectively. The superscript T, denoting the dielectric constant  $\epsilon_{ik}$ , is measured at constant stress. The subscripts  $i$  and  $k$  take the values 1, 2, 3 while  $j$  takes the values 1, 2, 3, 4, 5, 6 and the summation convention is used for repeated indices. The piezoelectric constant  $d_{ij}$  represents how electrical displacement, in charge per unit area, is related to the external force. For example,  $d_{33}$  is the proportional constant that describes the amount charge generated on the surfaces perpendicular to the direction of applied stress.

Piezoelectric sensors have very different characteristics to piezoresistive materials. They have less intrinsic thermal noise, which enables them to achieve better resolution and larger dynamic range. While piezoresistors are especially good at static measurements, piezoelectric sensors are capable of resolving vibration signals over a wide frequency range. Piezoelectric materials can also be made into modal sensors [50.17, 18], which are used to detect vibrations at specific frequencies. These characteristics of piezoelectric materials make them ideal candidates for vibration sensors at the MEMS scale. The chief disadvantages to piezoelectric sensing are complex processing requirements and the need for precise circuitry to condition and amplify the sensing signals if ultra-high resolution is desirable, as piezoelectric sensors are very sensitive to parasitic capacitances.

### 50.1.6 Electrostatic Microactuator Designs for Disk Drives

Various electrostatic microactuators have been designed for secondary actuation in HDDs. To incorporate an electrostatic microactuator into a HDD without altering much of the current suspension configuration, many design constraints are imposed. In this section, we will first discuss some design issues and then present one specific design example.

#### Translational Microactuators versus Rotary Microactuators

Depending on the motion of the magnetic head actuated, microactuator designs are categorized into two groups: translational actuators and rotary actuators. Either type can be implemented by comb-drive [50.8, 19] or parallel-plate [50.5, 6, 20] actuation.

When employing a translational microactuator in a dual-stage HDD servo, previous research [50.13] has shown that a force coupling between the suspension and the translational microactuator exists, consisting of transmitted actuation force from the VCM and suspension vibration induced by windage. The force coupling from the VCM not only complicates the dual-stage servo controller but also imposes a design constraint on a translational microactuator design, in that the translational microactuator has to provide a large force output to counterbalance the coupling force. When the VCM makes a large movement, as in seeking a new data track, the microactuator may be overpowered. One solution is to pull the actuator to one side and lock it momentarily in place. Even then, the use of the two actuation-stages must be carefully coordinated to mod-

erate the influence of the VCM on the microactuator. On the other hand, the linear springs in the translational microactuator can also aid in damping out motion of the suspension. The portion of suspension vibration induced by windage mostly consists of high-frequency excitation, so the resulting magnetic head's position error can be passively attenuated by low-resonant-frequency translational microactuators. This suppression makes translational microactuators preferable during track-following control.

Generally speaking, rotary actuators are more difficult to design/analyze than translational actuators because of their nonuniform gap between the shuttle and stator. Still, their different operating properties have both strengths and weaknesses. Unlike a translational actuator, no obvious force coupling is transmitted from the suspension to a rotary actuator, as the microactuator is nearly always attached to the end of suspension at the microactuator's center of rotation, which acts as a pivot point. With no mechanical coupling, the dual-stage servo system using a rotary microactuator does not suffer from the force coupling between VCM and microactuator seen in translational designs. However, the rotary microactuator has to compensate for the magnetic head's position error induced by suspension vibration without any passive attenuation of the vibration. Overall, a rotary actuator is likely to behave better than a translational microactuator during track seeking and worse during track following.

#### Gimballed Microactuator Design

Proper flying height and orientation of a slider and read/write head over a hard disk is maintained by the interaction of the suspension, the air bearing of the slider, and a gimbal structure. The gimbal structure is located at the tip of the suspension and holds the slider/microactuator in its center coupon. The dynamic characteristic requirements of gimbal structures are that they be flexible in pitch and roll motion but stiff to in-plane and out-of-plane bending motion. To meet all these requirements using only one piece of metal is a highly challenging task. For this reason, most commercially available suspension/gimbal designs consist of two to four pieces of steel, each with different thickness.

The goal of a gimballed microactuator design is to integrate an actuator and gimbal seamlessly into a one-piece structure, as shown in Fig. 50.7, to simplify both suspension design and HDD assembly. A fully integrated suspension that includes suspension, gimbal, and microactuators in one part has also been pro-

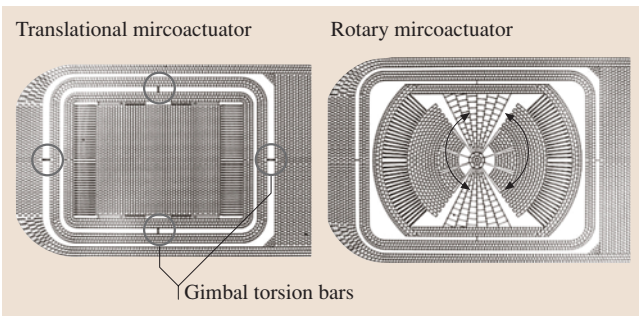


**Fig. 50.7** Schematics of translational microactuator versus rotary microactuator. Courtesy of Lilac Muller<sup>CE2</sup>

posed [50.21]. The dimple structure, existing in most current gimbal structures, is excluded from the gimballed microactuator design, and electrical interconnects are in situ fabricated on the gimballed microactuator, re-

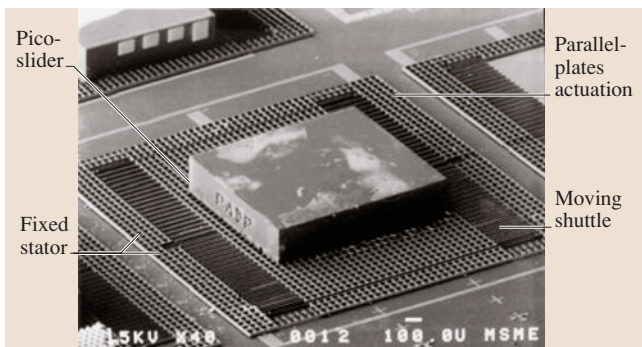


**Fig. 50.8** Pico-slider mounted on a translational microactuator. Courtesy of Horsley 1998<sup>CE2</sup>

placing the flexible cable in the current HDD suspension assembly.

The dimple structure in current suspension assemblies provides out-of-plane stiffness while preserving the necessary torsional compliance in the gimbal structure. Without a dimple structure in the suspension assembly, the gimbal itself must provide high out-of-plane bending stiffness. Otherwise, it would unbalance the suspension preload, which is an overbend of the suspension that balances the upward air-bearing force on the suspension during operation. The electrical interconnects are implemented to transmit data between magnetic heads, located at the center coupon of the gimbal structure, and IC<sup>CE3</sup> circuits located at the end of the suspension. The electrical interconnects fabricated in situ are inevitably passed through torsion bars of the gimbal and thus set a design constraint for the minimum width of the torsional bars. Furthermore, the gimbal structure and microactuator should be the same thickness to simplify the MEMS fabrication process.

To summarize the design constraints discussed above, the integrated gimbal structure has to meet performance requirements with a single, uniform piece of material that would previously have been achieved by two to four metal pieces with different thicknesses, while the minimum width of any torsion bars used is predetermined. To solve this problem, Muller [50.6] proposed a T-shaped structure (a beam structure with an overhanging surface sheet) for the torsion bars, and Chen [50.21] proposed double-flexured torsion bars. Additionally, many suspension manufacturers have developed new gimbal structures for their suspensions designed specifically for use with MEMS microactuators, moving

**Table 50.1** Parameters of the electrostatic microactuator design by Horsley 1998 [50.5]

Parameters	Source*	Value
Nominal gap	D	10 $\mu\text{m}$
Structure thickness	D	45 $\mu\text{m}$
Rotor mass, $m$	I	44 $\mu\text{g}$
$dC/dx$	C	68 fF/ $\mu\text{m}$
Actuation voltage, bias voltage	D	40 V
Actuation voltage, maximum driving voltage	D	$\pm 40$ V
Voltage-to-force gain, $K_v$	I	50 nN/V
Mechanical spring constant, $K_m$	I	29 N/m
Electrostatic spring constant, $K_e$	I	9.6 N/m
Damping coefficient, $b$	I	$1.03 \times 10^{-4}$ N/(m/s)
Voltage-to-position DC gain	M	0.05 $\mu\text{m}/\text{V}$
Resonance frequency, $w_r$	M	550 Hz

\* D = design value, C = calculation, M = measurement, I = inferred from measurements

<sup>CE3</sup> Please confirm definition of abbreviation IC on first use

the gimbal location back to the suspension from the microactuator.

**An Electrostatic Microactuator Design Example**

Figure 50.8 shows a translational microactuator design suitable for the HDD dual-stage actuation by *Horsley* in 1998 [50.5]. The translational electrostatic microactuator dimensions are 2.2 mm × 2.0 mm × 0.045 mm and the weight is 67 μg. The dimensions of the pico-slider on the top are 1.2 mm × 1.0 mm × 0.3 mm and the weight is 1.6 mg. This microactuator design does not include electrical-isolation features, and thus the electrical isolation and electrical interconnects were fabricated on a separate substrate and subsequently bonded to the microactuator. This microactuator uses parallel plates for the actuation force but does not have dedicated position-sensing structures due to fabrication process limitations. Table 50.1 summarizes the key parameters of this microactuator design.

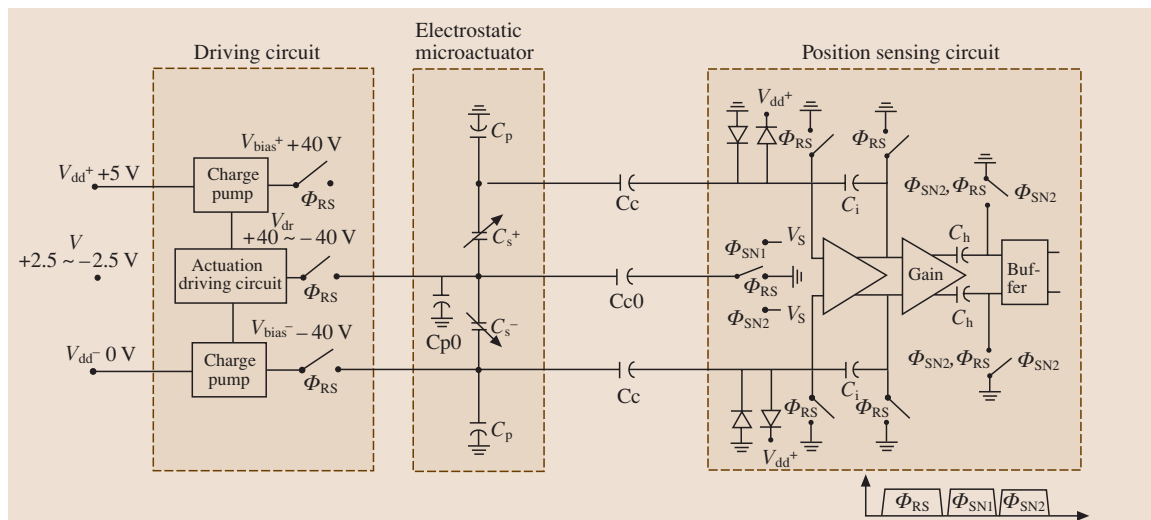
Based on these parameters, the characteristics of this electrostatic microactuator can be estimated by the linear differential equation shown in (50.6).

Figure 50.9 shows the schematics of a circuit design by *Wongkomet* in 1998 [50.14], in which the actuation driving voltage and capacitive position sensing were implemented for the electrostatic microactuator designed by *Horsley*. As mentioned before, the electrostatic microactuator design does not have a dedicated structure for a position sensing;

as a consequence, the input nodes for actuation and output nodes for capacitive position sensing have to share the same electrodes. The capacitors  $C_c$  and  $C_{c0}$ , shown in Fig. 50.9, are carefully designed to shield the high voltage presented in the actuation circuit from the sensing circuit, which is mostly low voltage, and thus enable driving/sensing circuit integration.

The driving circuit, shown in the left in Fig. 50.9, demonstrates how to generate the bias voltage ( $V_{bias}$ , ±40 V) and drive voltage ( $V_{dr}$ , -40–+40 V) from 0–5 V complementary metal oxide semiconductor (CMOS)-compatible circuits. The switches at the output of the charge pumps were synchronized with the switching period  $\phi_{RS}$ . During the sense phases  $\phi_{SN1}$  and  $\phi_{SN2}$ , therefore, the switches are left open and thus no voltage fluctuation is seen by the sensing circuits. This arrangement was utilized to reduce feed-through from the driving circuit to the position-sensing circuit.

The design target for the capacitive position-sensing circuit was to achieve a position-sensing resolution of 10 nm, and this goal was approached by two main techniques implemented in the circuit: differential sensing and correlated double sampling (CDS). The main benefits of the differential sensing scheme are reduced noise coupling and feed-through, elimination of even-order harmonics, and improvement of dynamic range by doubling the output swing. To adapt this differential sensing scheme in a differential parallel-plate electrostatic microactuator, a bias voltage ( $V_{bias}$ ) was applied



**Fig. 50.9** A simplified schematic including driving and sensing circuits for the electrostatic microactuator. Courtesy of Wongkomet 1998 [50.14]

<sup>4</sup> Please define abbreviation KT/C, or use algebraic format if appropriate

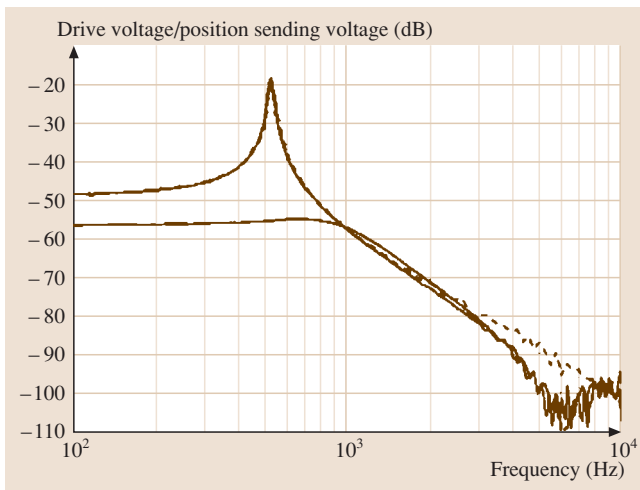


**Fig. 50.10** Open-loop and closed-loop frequency response of the prototype microactuator with a pico-slider. The capacitive position measurement (*solid line*) is compared to the measurements from LDV (*dashed line*). Courtesy of Wongkomet<sup>CE-2</sup>

to the stator and the drive voltage ( $V_{dr}$ ) was applied to the shuttle. The CDS technique, a modified capacitance-sensing technique based on the switched-capacitance scheme, was implemented along with the differential sensing scheme to compensate for sensing noises, including  $1/f$ ,  $KT/C$ <sup>CE-4</sup>, switch charge injection and offset from the op-amps [50.14]. The concepts of CDS can be briefly described as follows. The sense period is broken into three phases: one reset phase,  $\phi_{RS}$ , and two sense phases,  $\phi_{SN1}$  and  $\phi_{SN2}$ . During the  $\phi_{RS}$  sense phase, the voltages for the capacitors and input nodes to op-amps are set to the reference level of the DC-voltage setting for the charge integrator, the same as for the switched-capacitance scheme discussed in Sect. 50.1.4.

## 50.2 Fabrication

While there are several approaches to building electrostatic microactuators suitable for hard disk drives, they all exhibit certain common features from a fabrication standpoint.

### 50.2.1 Basic Requirements

As we discussed earlier, nearly all electrostatic microactuators rely on a system of interlaced fingers or plates to provide actuation force. As a result, a method for

During the  $\phi_{SN1}$  sense phase, a sensing voltage  $-V_s$  is applied to the shuttle and results in a voltage difference,  $\alpha(-V_s) + V_{error}$ , across the sampling capacitor  $C_h$ , where  $\alpha$  is the transfer function from the sense voltage to the output voltage at the preamplifier, shown as *Gain* in the plot, and  $V_{error}$  is the voltage at the output node of the preamplifier resulting from noise, leakage charge, and offset of op-amps. Lastly, during the  $\phi_{SN2}$  sense phase, the sensing voltage is switched from  $-V_s$  to  $V_s$  and the switch next to  $C_h$  is switched open. This results in a voltage output  $\alpha(V_s) + V_{error}$  at the output node of the preamplifier and a voltage,  $2\alpha(V_s)$ , at the input node of the buffer. As a consequence, the voltage resulting from the sensing error ( $V_{error}$ ), which appears at the output node of the preamplifier, disappears from the voltage-input node to the buffer. The switches utilized in the circuit and their corresponding timings are shown in Fig. 50.9. Be aware that, for simplicity of presentation, components in the preamplifier and buffer are not shown in detail in Fig. 50.9.

The frequency response, both open-loop and closed-loop with a PD<sup>CE-5</sup> controller, of the electrostatic microactuator measured by a capacitive position sensing circuit is shown in Fig. 50.10. The position measurements from an LDV<sup>CE-6</sup> are also shown in the same plot for comparison. The deviation between the measurements from the different position-sensing devices appears in the high-frequency region of the plot and has been identified as the feed-through from the capacitance-sensing circuit. The effect of feed-through was negligible in the low-frequency region but becomes significant at high frequencies and results in a deviation in magnitude for the transfer function of between  $-80$  dB and  $-90$  dB above 2 kHz. The feed-through presented in the capacitance-sensing circuits limited the position-sensing resolution to the level of 10 nm.

producing arrays of these fingers or plates with narrow gaps between them is usually the central concern in developing a fabrication process. The resulting structure must then be strong enough to support both the slider on the microactuator and the microactuator on the suspension, particularly when loaded by the air bearing that supports the slider above the hard drive's spinning disk. In addition, the design and fabrication process must include a way to perform electrical interconnection on the microactuator. This involves transferring signals

to and from the actuator and slider and isolating the parts of the microactuator that require different voltage levels.

Meanwhile, the microfabrication process is subject to certain basic constraints. The materials used in its fabrication must either be thermally and chemically compatible with any processing steps that take place after their deposition or must somehow be protected during steps that would damage them. This often constrains the choice of materials, deposition techniques, and processing order for microdevices. Another concern is that the surface of the structure be planar within photoresist spinning capabilities and lithography depth-of-focus limits if patterning is to be performed. This can be a major challenge for disk drive microactuators, which are large in size and feature high-aspect-ratio trenches compared to other MEMS devices.

### 50.2.2 Electrostatic Microactuator Fabrication Example 1

Section 50.1.5 described the design and operation of a translational electrostatic microactuator. This section examines the fabrication process by which that microactuator was built [50.5]. The process is a variation on a micromolding process known as HexSil [50.22]. In a micromolding process, a mold wafer defines the structure of the microactuator and may be reused many times like dies in macro-scale molding; in the HexSil version of the procedure, the mechanical parts of the microactuator are formed in the mold by polysilicon. A second wafer is used to create metalized, patterned target dies. Upon extraction from the mold, the HexSil structure is bonded to this target substrate, which is patterned to determine which sections of the HexSil structure are electrically connected.

Naturally, the mold wafer is the first item to be processed and is quite simple. It is a negative image of the desired structure, etched down into the wafer's surface, as shown in Fig. 50.11a. A deep but very straight etch is critical for successful fabrication and subsequent operation of the devices. If the trench is too badly bowed or is undercut, the finished devices will become stuck in the mold and difficult to release. On the other hand, a tall device will have a larger electrostatic array area, will generate more force, and be better able to support a slider while in a disk drive.

Fabrication of the HexSil structure forms the majority of the processing sequence Fig. 50.11b–g. HexSil fabrication begins by coating the surface of the mold wafer with a sacrificial silicon oxide. This layer, de-

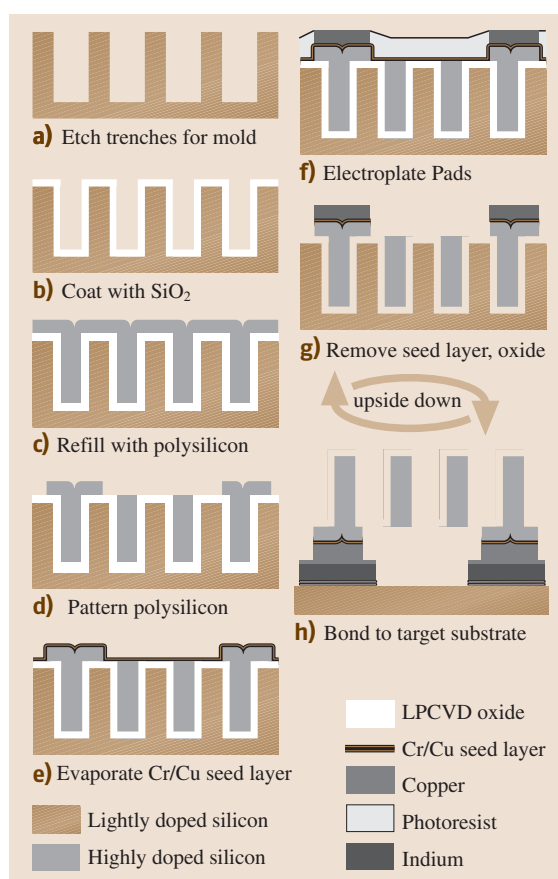


Fig. 50.11 Fabrication example 1: HexSil

posited by low-pressure chemical vapor deposition (LPCVD), must coat all surfaces of the mold, so that removal of the oxide at the end of the process will leave the device completely free of the mold. This microactuator uses a 3–4 μm-thick oxide layer to ensure clearance between the polysilicon structure and the trench walls during release. The mold is then refilled completely with LPCVD polysilicon, which will form the desired mechanical structure. Polysilicon is chosen for its conductivity and good conformality in refilling trenches. This also leaves a planar surface ready for photolithography to cover the bonding locations. After the lithography step, the polysilicon deposited on top of the wafer is removed except where the bonding points were defined.

The structure is then prepared for bonding by forming a soldering surface. First a chrome/copper seed layer is evaporated onto the surface of the wafer. The chrome promotes copper adhesion to the silicon, while the cop-

per forms the starting point for electroplating. The seed layer is covered with photoresist, which is cleared only in the locations where contacts are desired. There, electroplating will produce a metal film, forming soldering points for the device to the target substrate that will form its base. In this case, copper is used as the plating material, thanks to its high conductivity and solderability. The device is released from the mold by ion milling away the thin seed layer, then dissolving the oxide lining with a hydrofluoric (HF) acid wet etch. The free-standing portion of the microactuator is thus ready for bonding to the target. The mold, meanwhile, may be used again after a simple cleaning step.

The target substrate may be prepared in several ways. The target shown above consists simply of indium solder bumps and interconnects on a patterned seed layer; this is known as a *plating bus* arrangement. The seed layer is used for the same reasons as on the HexSil structure, but in this case the seed layer is patterned immediately, with the unwanted portions removed by sputter etching. This provides isolation where desired without having to etch the seed layer after the indium is in place. Photoresist is spun again and patterned to uncover the remaining seed layer. A layer of indium is then electroplated everywhere the seed layer is visible. Indium acts as the solder when the two parts of the microactuator are pressed together, forming a cold weld to the copper at 200–300 MPa, as shown in Fig. 50.11h, that was found suitable for hard disk requirements.

### 50.2.3 Electrostatic Microactuator Fabrication Example 2

The high-aspect ratio microactuator described in this section is in development at the University of California, Berkeley, and demonstrates another way to create the features required of an actuated slider. The microactuator is translational, with parallel-plate actuation, and includes two of the design options described previously: integrated isolation plugs, as described in Sect. 50.1.3, and a capacitive sensing array, as described in Sect. 50.1.4. A picture of the basic design is shown in Fig. 50.12; a central shuttle holding the slider is supported by four folded-flexure springs and driven by parallel-plate arrays.

#### Basic Process: Silicon-on-Insulator

Successful processing of the design is centered around the ability to etch very straight, narrow trenches using deep reactive-ion etching (DRIE). DRIE is a special plasma etching sequence that uses polymerization of the sidewalls of a trench to keep the walls straight even at extreme aspect ratios. Deep, narrow trenches make possible a microactuator with both closely packed electrostatic arrays and good mechanical strength. Conventional surface micromachining is used to produce the majority of the electrical interconnects.

The basic fabrication process uses a silicon-on-insulator (SOI) wafer to control the DRIE trench depth. SOI wafers are very useful in microfabrication as they provide a layer of single-crystal silicon (the device layer) separated from the bulk of the wafer (the handle layer) by a thin layer of buried silicon oxide. This gives a very well-controlled thickness to the finished device but is very expensive. The microactuators described here are fabricated from an SOI wafer with a 100 μm device layer. A variation on the processing sequence and layout eliminates the need for SOI wafers and will be discussed in the following section.

The first stage of fabrication is the creation of deep isolation trenches (see Fig. 50.13a–c). This procedure has been adapted to MEMS from integrated circuit processing for isolating thick MEMS structures [50.23]. The isolation pattern is formed by photolithography and etched by DRIE down to the buried oxide. With trenches only 2 μm wide, this corresponds to an aspect ratio of 50 : 1. The wafer surface and trenches are then coated with LPCVD silicon nitride, which acts as the electrical insulator. The trench is then refilled in its entirety with LPCVD polysilicon, which is a more conformal material that better fills the trench than silicon nitride would

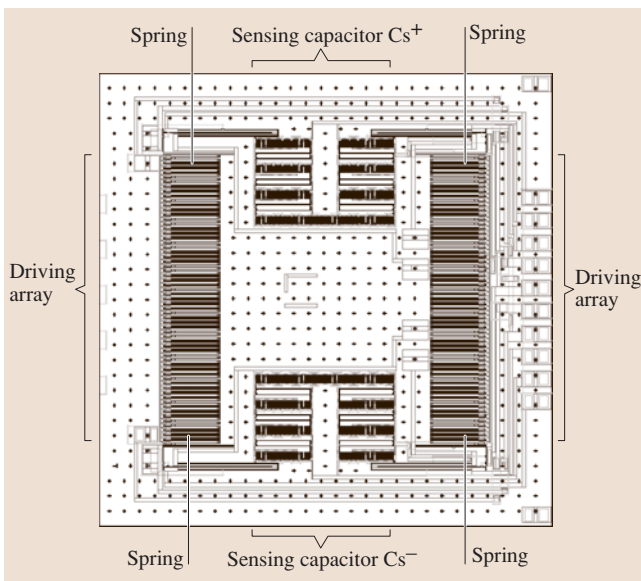
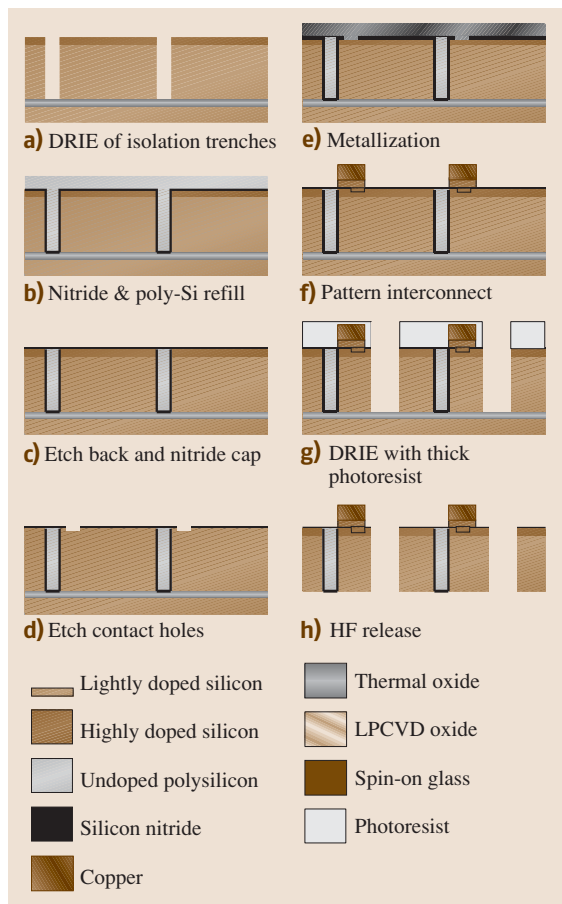


Fig. 50.12 Translational high-aspect-ratio microactuator

alone; polysilicon also has much lower residual stresses than silicon nitride. The refill leaves a layer of polysilicon on the surface of the substrate, which must be etched or polished back to the silicon nitride. After etch-back, a second layer of LPCVD nitride completes the isolation between regions.

Next, electrical interconnects are formed, as shown in Fig. 50.13d–f. Contact holes to the substrate are defined by photolithography and etched by reactive-ion etching of the silicon nitride. Metal lines may then be patterned directly by photolithography or formed by lift-off. In a lift-off process, photoresist is deposited and patterned before the metal. The metal is then deposited vertically, so that the sidewalls of the resist are uncovered. Dissolving the resist allows the metal on top to float away, leaving behind the interconnect pattern. In the figures shown here, the interconnects are formed by a metal/polysilicon stack.



**Fig. 50.13** Basic silicon-on-insulator fabrication process

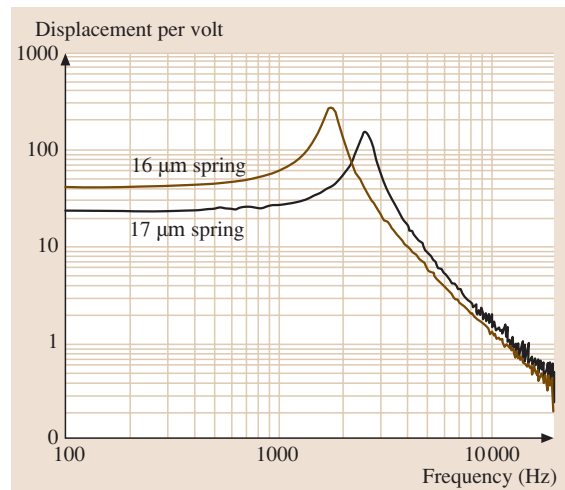


**Fig. 50.14** Dynamic response of microactuators from SOI wafer with 16 μm and 17 μm spring widths

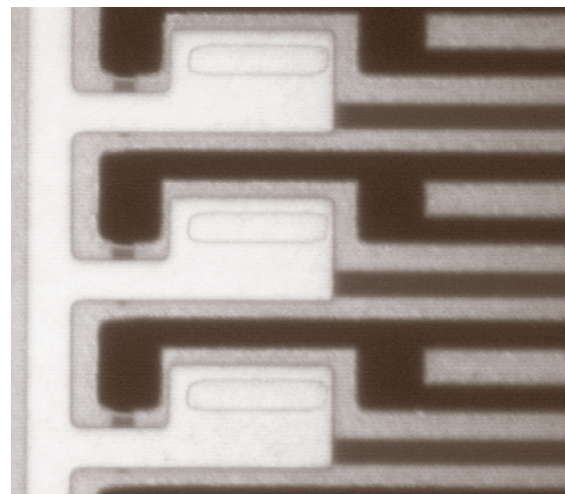


**Fig. 50.15** Electrostatic driving array of microactuator from SOI

A highly doped polysilicon layer provides a robust base layer for the interconnects, while the overlying metal keeps <sup>CE7</sup>. The ability to isolate portions of the substrate is useful for simplifying the interconnect layout, as one interconnect can cross another by passing underneath it through an isolated portion of the substrate.

Finally, structural lithography is performed and a second etch using DRIE is done, as shown in Fig. 50.13g. These trenches will define the shape of the microactuator, and are larger, 4 μm wide, to allow suf-

<sup>CE7</sup> Please complete this sentence fragment

efficient rotor travel. After this etch step, the device layer on the SOI buried oxide consists of fully defined microactuators. When the buried oxide is removed by wet etching, the microactuator is released from the substrate Fig. 50.13h and, after removal of the photoresist that protected the device surface from the HF during release, is ready for operation.

Microactuators fabricated using the above process have been installed into a disk drive test assembly for dual-stage controller evaluation. The frequency responses of two such microactuators, with two different spring sizes, are shown in Fig. 50.14. Microactuator resonant frequencies range from 1.7 to 2.6 kHz. Thanks to the high-aspect-ratio processing made possible by DRIE, static displacement gains as large as 200 nm/V are observed, with high-frequency gains exceeding 1 nm/V past 10 kHz. A picture of the electrostatic structure used to drive this motion, with rotor fingers on the right and stator fingers on the left, divided down the center by isolation trenches, is shown in Fig. 50.15.

An alternative fabrication approach is to build the microactuator from a regular silicon wafer ( $\approx 550 \mu\text{m}$  thick), but then, since the microactuator should not be more than  $100 \mu\text{m}$  thick to fit in a HDD, etch away the back side of the wafer to obtain devices of that size. The main reason for using a silicon-only wafer is to reduce the need for expensive SOI wafers, which cost approximately ten times as much as single-material wafers. Another benefit is the elimination of the need for etch holes to reach the buried oxide layer, which increase the vulnerability of microactuators to particle or moisture contamination. However, the thickness of the devices cannot be controlled as accurately as with the SOI process, and the processing sequence is more complicated.

Control of back-side etching is difficult, making it hard to obtain devices with uniform thickness across a wafer. A proposed solution is to use an anisotropic wet etchant during the back-side etch step. Anisotropic etchants work very slowly on certain crystal planes of a single-crystal silicon wafer; a coating on trench sidewalls can protect fast-etching planes when the etchant reaches the trenches from the back, causing slow-etching crystal planes to begin to come together, which slows the etch. The result is a nearly self-stopping etch with a V-shaped profile that prevents overetching even in the presence of nonuniformities in etch rate and trench depth across the wafer. The most common anisotropic etchants are potassium hydroxide (KOH) and tetramethyl ammonium hydroxide (TMAH). This release process is

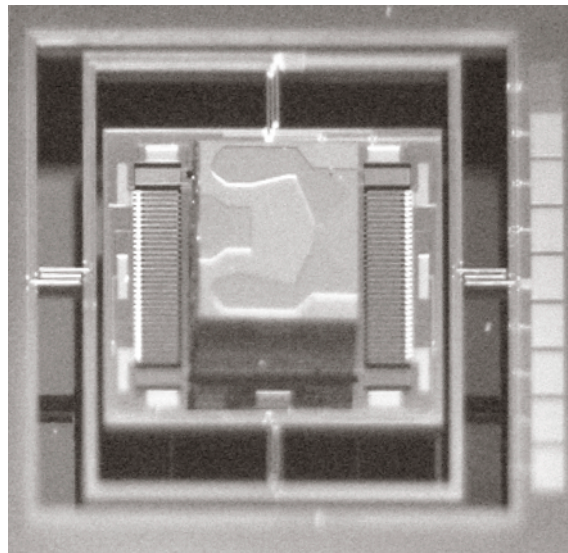


**Fig. 50.16** Microactuator with integrated gimbal fabricated by ABR

referred to here as an anisotropic back-side release (ABR).

The key to a good release by this method is to provide reliable protection of the top of the wafer and the deep trenches from the etchant. The most effective etch barriers are silicon nitride (for KOH or TMAH) or thermally grown silicon oxide (for TMAH). However, these films are typically deposited using high-temperature processes, which preclude the use of most metals. Microactuators produced by this method have a similar process flow to those described in the previous section, but the metal layer of the surface interconnects is omitted, as shown in Fig. 50.14a. The wafers are then coated with silicon nitride, which is removed from the back side of the wafer by plasma etching. An anisotropic etchant removes the bulk of the silicon wafer, and finally the protective nitride is removed from the front side of the wafer using HF acid.

A prototype microactuator with integrated gimbal fabricated using ABR is shown in Fig. 50.16. This prototype was operated with a 30 V DC bias and  $\pm 8$  V AC driving voltage for  $\pm 1 \mu\text{m}$  displacement.

#### 50.2.4 Other Fabrication Processes

Where the DRIE-based process described above *digs* the microactuator out of a wafer, a procedure developed by IBM *grows* a microactuator with high-aspect-ratio trenches on top of a wafer [50.24].

electroplated microactuator  
metal!seed layer  
suspension-level fabrication  
PZT (lead zirconate titanate)!actuated suspen-  
sions  
integrated!silicon suspension  
integrated!suspension

Index entries on this page

### IBM Electroplated Microactuator

The microactuator is fabricated by a clever sequence of electroplating steps and sacrificial depositions. A sacrificial oxide film is first patterned then covered with a metal seed layer. When later removed, the sacrificial film will have left a gap between the microactuator and substrate portions of the microactuator needed to move freely. A polymer, 40  $\mu\text{m}$  thick, is spun onto the wafer and patterned with a reverse image of the main structural layer. Trenches are etched down to the sacrificial layer by plasma etching then refilled by electroplating, much like micromolding. Another sacrificial polymer, a photoresist this time, separates the top of the fixed portions of the structure from the platform upon which the slider will sit, while conveniently planarizing the surface for further lithography. The platform is created by two more electroplating steps on top of the parts of the structure that will move freely. Removal of the sacrificial layers (photoresist, polymer, and oxide) releases the microactuator for use.

This process has been used to produce both rotary and linear microactuators and is comparatively advanced from a commercial standpoint. The resulting devices are thinner than those described in the previous example, but a similar aspect ratio (20 : 1) can be achieved. This procedure also has the benefits of being a low-temperature process, which helps decrease processing cost and is compatible with the thin-film magnetic-head manufacturing process. Moreover, it includes an upper structure that covers the fingers, which improves device reliability by shielding the fingers from particles.

Additional fabrication details and dynamic testing results for the IBM design may be found in references [50.24] and [50.25]. A microactuator fabricated by this process has demonstrated an open-loop bandwidth of 8 kHz after installation into a hard disk drive [50.26]. Certain closed-loop control results for such a microactuator are described in Sect. 50.3.2.

### Electroplated Microactuators with Fine Gaps

Finally, fabrication processes developed at the University of Tokyo demonstrate additional techniques for obtaining very small gaps between electrostatic fingers [50.27]. Similar to the IBM process, electrostatic fingers are electroplated, in this case by nickel, within a polymer pattern. The gap between closely spaced fingers, however, is then formed by a sacrificial metal. Photoresist is used to cover the fingers except for the surfaces where a small gap is desired; these are electroplated with sacrificial copper, making narrow, well-defined gaps possible, in perhaps the most reliable of the pro-

cesses described here. Continuing with a second nickel electroplating step creates the interlaced fingers, which will also support the slider; the wafer is polished down to the level of the structure. Finally the copper, photoresist, and seed layer are etched away, leaving the free-standing structure.

In another version of process, photoresist alone separates the stator and rotor fingers. In this case, a thin layer of photoresist is left where small gaps are desired, instead of growing a layer of copper. This method is dependent on excellent alignment but can eliminate the need for polishing after the second electroplating step.

### 50.2.5 Suspension-Level Fabrication Processes

The long, highly integrated fabrication processes required by actuated slider microactuators contrast greatly with the fabrication of actuated suspension microactuators and instrumented suspension, though the material requirements and environments of the suspension add interesting challenges to the use of such devices.

#### PZT Actuated Suspensions

In most cases, actuated suspensions use piezoelectric (lead zirconate titanate, PZT) drivers cut or etched as single, homogeneous pieces and attached to the steel suspension. Nevertheless, microfabrication techniques can still be useful in suspension processing. For example, some recent suspensions have used thin-film PZT deposited on a substrate by sputtering or spinning on of a sol-gel for incorporation in a suspension. This is intended to produce higher-quality PZT films and begins to introduce MEMS-style processing techniques even into suspension-scale manufacturing [50.28, 29].

#### Integrated Silicon Suspension

Another area where silicon processing has been suggested for use on a suspension is the gimbal region, or even the entire suspension, as described in [50.21]. An integrated silicon suspension would incorporate aspects of both actuated suspension and actuated slider fabrication. Force is provided by four pieces of bulk PZT cut down to size, as in other actuated suspensions, but the rest of the suspension is fabricated from single-crystal silicon by bulk micromachining.

The fabrication process for the integrated suspension is the precursor to the ABR process used to fabricate the microactuator in Sect. 50.2.3. Layers of LPCVD silicon nitride and polysilicon are deposited on bare silicon wafers. The polysilicon is doped by ion implantation

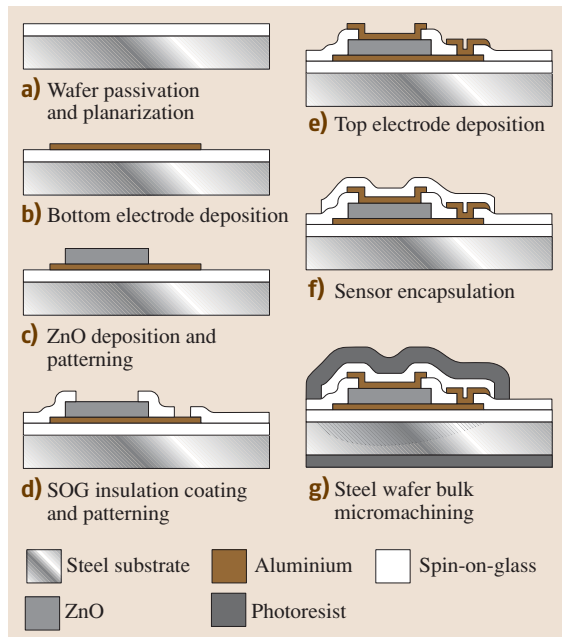


**Fig. 50.17** Fabrication process for a zinc oxide sensor on a steel substrate

and covered with a second layer of nitride. The outline of the suspension and any spaces within it are then lithographically patterned. After a reactive-ion nitride etch to reach the substrate, trenches are etched by DRIE. The trenches are then plugged with spin-on polymer for further lithography. First, the top layer of polysilicon is patterned into piezoresistive strips for sensing vibration. Second, a layer of photoresist is patterned for copper lift-off, to create metal interconnects. Last, the planarizing polymer is removed, and the entire surface is coated with silicon nitride. This final coating protects the top surface during an anisotropic back-side wet etch, in this case by potassium hydroxide.

#### Instrumented Suspensions

Finally, microfabrication techniques may be useful for installing sensors on conventional steel suspensions, in order to help a microactuator suppress suspension vibration. Strain gages located at key points on the suspension can detect structural vibrations of the suspension. These measurements may be fed forward to a microactuator at very high sampling rates, and used to cancel out the vibration at the read/write head. For effective operation, the strain gages must detect strain levels on the order of 10s of nanostrain, requiring highly sensitive sensor materials, such as those used in microfabrica-

tion on silicon wafers. Because the sensors are built on steel substrates to be assembled in suspensions, however, only low-temperature, low-stress microfabrication processes are permissible. This complicates sensor fabrication, as does the comparatively rough surface of steel wafers. In addition, the performance of sensors on a disk drive suspension is very sensitive to sensor placement, as discussed in [50.30–32].

Two types of strain sensors are currently under development: piezoresistive strain sensors and piezoelectric strain sensors. The critical step in sensor fabrication is the addition of a strain-sensitive material under the temperature and stress constraints imposed by fabrication on steel. In either case, processing begins with the deposition of an insulating film to isolate the sensors electrically from the steel substrate. Possible materials include spin-on glasses, polymer films, or metal oxides. Sensors must also include metal interconnects to provide electrical connections to an external controller, typically implemented through metal evaporation and patterning or lift-off.

The function of piezoresistive strain gages is relatively simple, and was discussed in Sect. 50.1.4. To build such sensors on a steel substrate, the simplest procedure is to deposit a piezoresistive film directly onto the wafer. For instance, doped polysilicon may be sputtered onto steel at low temperatures with low residual stress. Unfortunately, such a film has a very high resistivity, resulting in a very large source of thermal noise. Alternatively, high-quality sensors may be built separately from any piezoresistive material, such as single-crystal silicon, then installed on the steel substrate using metal-on-metal bonding, but this process is very expensive.

A very promising alternative to piezoresistive strain gages is piezoelectric vibration sensors. As described in Sect. 50.1.4, piezoelectric materials are very good at detecting extremely small dynamic signals. In order to fabricate piezoelectric sensors directly on steel wafers, however, it is important to choose a material that has good microfabrication compatibility in addition to good piezoelectric properties. Thermal-coefficient mismatch between steel substrates and all nonmetal materials is especially constraining for piezoelectric materials, as it limits the maximum permissible temperature over the course of the fabrication process. A survey shows that the most well-known piezoelectric material lead zirconate titanate (PZT) does not provide sufficient process compatibility. Not only is it difficult to deposit, but it also requires high temperatures for curing and polarization. Aluminum nitride, a material commonly used to build MEMS devices, has much better fabri-

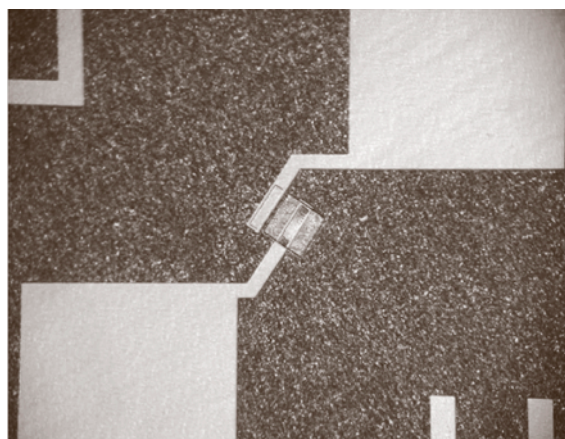


**Fig. 50.18** Piezoelectric strain sensor on steel substrate

compatibility but still requires relatively high temperatures for deposition. For instrumented suspensions, zinc oxide (ZnO) has been identified as having good process compatibility and decent piezoelectric properties.

Zinc oxide sensor fabrication, shown in Fig. 50.17 starts with putting a spin-on glass (SOG) layer onto a bare steel wafer. The SOG layer serves as an electrical-insulation layer between the steel substrate and the sensors, while also planarizing the rough steel surface and preventing steel from oxidizing during processing. Next, an aluminum layer is evaporated and patterned to form the bottom electrode of the sensor. Then, a ZnO layer is sputtered and patterned onto the electrode, followed by the second SOG coating as another insulation layer. Using the bottom electrode and ZnO as etch stoppers, the contact holes are opened through the SOG layer using reactive-ion etching (RIE). Another metal layer is then deposited to form the top electrode and leads. To prevent leads from shorting out accidentally during operation, the last SOG layer is coated on the wafer to encapsulate the sensor and leads. After the fabrication of the sensors, two more etching steps are needed to transform steel wafers into suspension parts. First, the residual SOG has to be cleared out so that steel is exposed for welding during suspension assembly. Secondly, the wafer is patterned into suspension parts and bulk micro-machining is performed to etch through the wafer, leaving suspension geometries at the end. The cross section of a sensor built by this method is shown in Fig. 50.17. A picture of a ZnO piezoelectric sensor, 200 μm by 200 μm in area and 0.8 μm thick, is shown in Fig. 50.18. Slightly larger sensors, 300 μm by

300 μm, have demonstrated strain resolutions down to 50 nanostrain.

### 50.2.6 Actuated Head Fabrication

Several interesting fabrication processes have been proposed for another approach to creating a dual-stage disk drive servo: the actuated head. In an actuated head, the actuator is built into the slider and moves just the read/write head. This could potentially eliminate many of the mechanical limits of actuated suspensions or actuated sliders. Actuation techniques are typically similar to those of actuated sliders, with the key complication being the need to integrate an actuator fabrication process with a slider fabrication process. We discuss ways in which this might be done below.

One fabrication approach to actuating a read/write head is to enclose an electrostatic driving array inside a slider. The slider is built on a glass or silicon substrate, beginning with the air-bearing surface (ABS), followed by a microactuator, and then surrounded by the remainder of the slider. The ABS is formed by silicon oxide deposited over aluminum and tapered photoresist layers that give it a contoured shape. The majority of the ABS is then covered with photoresist, while a block in the center is plated with nickel and etched to form the electrostatic actuator. The electrostatic microactuator, in turn, is covered while the remainder of the slider body is electroplated. The slider may then be bonded to a suspension and the ABS surface released from the substrate by etching away the original aluminum and photoresist surface [50.9].

The sacrificial metal technique described in Sect. 50.2.4 is another possibility for building an electrostatic array onto a slider. It can be used to form a small array with very narrow gaps, and the process is compatible with slider and head materials [50.33].

The third actuated-head process makes use of an SOI wafer and silicon-based materials. For this structure, a 20 μm device layer is coated with silicon nitride. The nitride is patterned with contact holes for connections to the substrate and used as insulation over the rest of the device. A layer of molybdenum is sputter-deposited to perform interconnections to both the head and the electrostatic array. This array is formed by DRIE to the buried oxide, using a lithographically patterned hard mask of tetraethylorthosilicate. The result is a simple, tiny, actuator that must be bonded to the edge of a slider after release from the SOI wafer [50.34].

## 50.3 Servo Control Design of MEMS Microactuator Dual-Stage Servo Systems

The objective of disk drive servo control is to move the read/write head to the desired track as quickly as possible, referred to as track-seek control, and, once on-track, position the head on the center of the track as precisely as possible, referred to as track-following control, so that data can be read/written quickly and reliably. The implementation of the servo controller relies on the position error signal (PES), which is obtained by reading the position information encoded on the disk's data tracks.

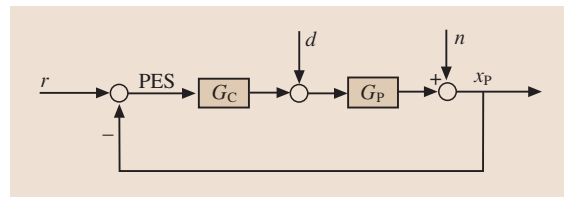


Fig. 50.19 Disk-drive servo control

### 50.3.1 Introduction to Disk Drive Servo Control

The position error is also called track misregistration (TMR) in the disk drive industry. Major TMR sources in the track-following mode include spindle runout, disk fluttering, bias force, external vibration/shock disturbance, arm and suspension vibrations due to air turbulence, PES noise, written-in repeatable runout, and residual vibration due to seek/settling [50.35]. These sources can be categorized as runout,  $r$ , input disturbance,  $d$ , and measurement noise,  $n$ , by the locations they are injected into the control system, as shown in Fig. 50.19. In Fig. 50.19,  $G_P(s)$  and  $G_C(s)$  represent the disk drive actuator and the controller, respectively;  $r$  and  $x_p$  represent track runout and head position, respectively.

From Fig. 50.19, the PES can be written as

$$\text{PES} = S(s)r + S(s)G_P(s)d - S(s)n, \quad (50.10)$$

where  $S(s)$  is the closed-loop sensitivity function defined by

$$S(s) = \frac{1}{1 + G_C(s)G_P(s)}. \quad (50.11)$$

The higher the bandwidth of the control system, the higher the attenuation of the sensitivity function  $S(s)$  below the bandwidth. Thus, one of the most effective methods to reduce PES and increase servo precision is to increase the control system bandwidth.

Traditional disk drive servo systems utilize a single voice coil motor (VCM) to move the head. Multiple structural resonance modes of the E-block arm and the suspension located between the pivot and the head impose a major limitation on the achievable control bandwidth. A dual-stage servo system using a MEMS actuated-slider microactuator can achieve high bandwidth because the microactuator is located between the

suspension and the slider, so actuation of the microactuator does not suffer from the resonance of the pivot, E-block, and suspension. Cooperation of a VCM and a MEMS microactuator thus provides the possibility of achieving higher servo bandwidth.

When the MEMS microactuator is translational, it even has the capability of filtering out those structural resonance modes. This feature is preferable and even crucial when the PES has been reduced down to the order of a few nanometers ( $1 - \sigma$ ) and airflow-excited suspension vibrations have become a significant component in TMR. As a solution, an instrumented suspension can be employed, and vibration information from the suspension can be fed to the VCM for feedback damping, or to the microactuator for feed-forward compensation.

One basic task of dual-stage servo control design is to increase the control bandwidth using the second-stage actuator. Many design methodologies have been developed to accomplish this objective. In this section, we first review major dual-stage servo control design methodologies, and then we discuss design considerations for controller design of a MEMS microactuator dual-stage servo system. As design examples, the details of track-following control designs using a sensitivity-function-decoupling design method and the mixed  $H_2/H_\infty$  design method are presented in Sect. 50.3.3. A comprehensive approach to robust control using a multi-rate controller is described in Sect. 50.3.4. In Sect. 50.3.5, we introduce a short-span seek control scheme using a dual-stage actuator based on decoupled feed-forward reference-trajectory generation.

### 50.3.2 Overview of Dual-Stage Servo Control Design Methodologies

Various control design architectures and methodologies have been developed for dual-stage servo control design. They can be largely classified into two categories: those based on decoupled or sequential single-input single-

output (SISO) designs, and those based on modern optimal design methodologies, such as linear quadratic Gaussian (LQG), LQG/loop-transfer recovery (LTR),  $H_\infty$ ,  $\mu$ -synthesis, and mixed  $H_2/H_\infty$  in which the dual-stage controllers are obtained simultaneously.

Two constraints must be considered in dual-stage servo control design. First, the contribution from each actuator must be properly allocated. Usually the first-stage actuator, or the coarse actuator, has a large moving range but a low bandwidth while the second-stage actuator, or the fine actuator, has a high bandwidth but small moving range. Second, the destructive effect, in which the two actuators fight each other by moving in opposite directions, must be avoided.

#### Classical SISO Design Methodologies

Several architectures and design methodologies have been proposed to transform the dual-stage control design problem into decoupled or sequential multiple SISO compensator design problems, for example, master–slave design, decoupled design [50.36], *PQ* method [50.37], and direct parallel design [50.38]. Figures 50.20–50.23 show the block diagrams of dual-stage controller designs using these methods. In these figures,  $G_1$  and  $G_2$  represent the coarse actuator (VCM) and fine actuator (microactuator) respectively;  $x_1$  is the position of the coarse actuator;  $x_r$  is the position of the fine actuator relative to the coarse actuator;  $x_p$  is the total position output;  $r$  is the reference input (runout), and PES is the position error,  $e = r - x_p$ .

**Master–Slave Design.** In a traditional master–slave structure, the absolute position error is fed to the fine

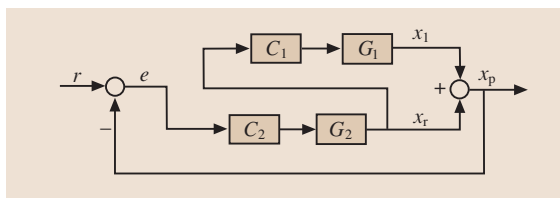


Fig. 50.20 Master–slave design structure

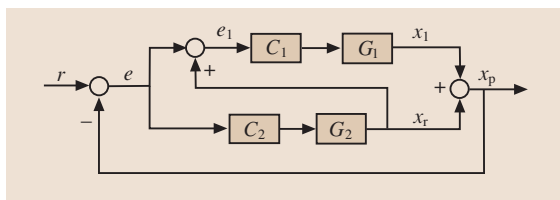


Fig. 50.21 Decoupled control design structure

actuator, and the output of the fine actuator is fed to the coarse actuator, as shown in Fig. 50.20. The position error will be compensated by the high-bandwidth fine actuator. The coarse actuator will follow the fine actuator to prevent its saturation.

**Decoupled Design.** Figure 50.21 shows the decoupled design structure [50.36], which is similar to the master–slave structure. A summation of the fine actuator output and the position of the coarse actuator is fed the coarse actuator. A very nice feature of this structure is that the control system is decoupled into two independent control loops, and the total sensitivity function is the product of the sensitivity functions of each of the control loops [50.13]. Thus the two compensators  $C_1$  and  $C_2$  can be designed independently. Decoupled design is also referred to as decoupled master–slave design, or sensitivity-function-decoupling design. In Sect. 50.3.3, details of a track-following controller designed using this method will be <sup>8</sup>CE.

Both the master–slave and the decoupled designs use the relative position of the fine actuator,  $x_r$ . If a relative position sensor is unavailable,  $x_r$  can be estimated using a model of the fine actuator.

***PQ* Design Method.** The *PQ* method is another innovative design technique for control design of dual-input single-output systems [50.37]. A block diagram of a dual-stage control design using this method is shown in Fig. 50.22.

In *PQ* design,  $P$  is defined by

$$P = \frac{G_1}{G_2}, \quad (50.12)$$

and a dual-stage controller can be designed in two steps. The first involves the design of an auxiliary compensator  $Q$  for plant  $P$ , which is defined by

$$Q = \frac{C_1}{C_2}. \quad (50.13)$$

$Q$  is designed to parameterize the relative contribution of the coarse and fine actuators. The 0 dB crossover

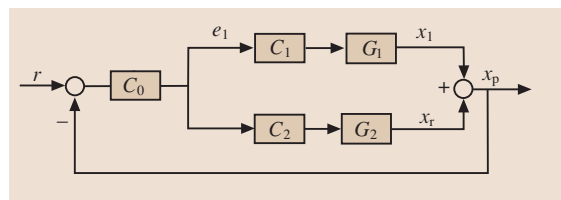
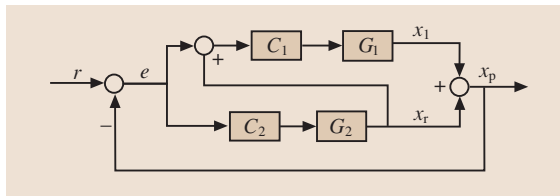


Fig. 50.22 *PQ* control design structure

<sup>8</sup>CE Please complete this sentence



**Fig. 50.23** Parallel control design structure

frequency and phase margin of the open-loop transfer function  $PQ$  are the design parameters in the design of  $Q$ . At frequencies below the 0 dB crossover frequency of  $PQ$ , the output is dominated by the coarse actuator, while at frequencies above the 0 dB crossover frequency, the output is dominated by the fine actuator. At the 0 dB crossover frequency, the contributions from the two actuators are equal. A large phase margin of  $PQ$  will ensure that the two actuators will not fight each other when their outputs are close in magnitude, thus avoiding any destructive effects.

The second step in the  $PQ$  design methodology is to design a compensator  $C_0$  for the SISO plant  $PQ$  such that the bandwidth (crossover frequency), gain margin, phase margin, and error rejection requirements of the overall control system are satisfied.

**Direct Parallel Design.** It is also possible to design the dual-stage controller directly using a parallel structure, as shown in Fig. 50.23, by imposing some design constraints and by sequential loop closing [50.38].

The two constraints for parallel design in terms of the PES open-loop transfer functions are [50.38]:

$$C_1(s)G_1(s) + C_2(s)G_2(s) \rightarrow C_2(s)G_2(s), \quad (50.14)$$

at high frequencies and

$$|C_1(s)G_1(s) + C_2(s)G_2(s)| \gg |C_2(s)G_2(s)|, \quad (50.15)$$

at low frequencies. The first constraint implies that the open-loop frequency response of the dual-stage control system at high frequencies approximately equals that of the fine-actuator control loop. Thus the compensator  $C_2(s)$  can be first designed independently as a SISO design problem to satisfy the bandwidth, gain margin, and phase margin requirements of the dual-stage control system. The second constraint ensures that the fine actuator will not be saturated. Compensator  $C_1(s)$  can then be designed for the SISO plant model with the fine-actuator control loop closed, such that the low-frequency constraint and overall stability requirement are satisfied.

This model is defined by:

$$G(s) = \frac{G_1(s)}{1 + C_2(s)G_2(s)}. \quad (50.16)$$

A dual-stage controller for a MEMS dual-stage actuator servo system has been designed using this method and implemented at IBM. An open-loop gain-crossover frequency of 2.39 kHz with a gain margin of 5.6 dB and a phase margin of  $33^\circ$  was obtained. In experimental testing, a 1- $\sigma$  TMR of  $0.024 \mu\text{m}$  has been achieved [50.38].

#### Modern MIMO Design Methodologies

Since the dual-stage actuator servo system is a MIMO system, it is natural to utilize modern MIMO optimal design methodologies, such as LQG, LQG/LTR,  $H_\infty$ , and  $\mu$ -synthesis, to design the dual-stage controller. Usually MIMO optimal designs are based on the parallel structure shown in Fig. 50.23, augmented with noise/disturbances models and other weighting functions to specify the control design performance objectives.

Linear quadratic Gaussian (LQG) control combines a Kalman filter and optimal state feedback control based on the separation principle. However, the Kalman filter weakens the desirable robustness properties of the optimal state feedback control. Linear quadratic Gaussian/loop-transfer recovery (LQG/LTR) control recovers robustness by a Kalman filter redesign process. Examples of dual-stage control designs using LQG and LQG/LTR have been reported in [50.39–41].

$\mu$ -synthesis design methodology is based on  $H_\infty$  design and further accounts for plant uncertainties during the controller synthesis process with guaranteed robustness. In  $\mu$ -synthesis, system performance is characterized by the  $H_\infty$  norm of the system. However, system performance can be more naturally characterized by the root-mean-square (RMS) value of PES, which is reduced to an  $H_2$  optimization problem, like the LQG controller. In the mixed  $H_2/H_\infty$  design approach, system performance is formulated as an  $H_2$  norm, and bounds are imposed to guarantee stability robustness to plant uncertainties. Example of dual-stage control designs using  $H_\infty$ ,  $\mu$ -synthesis and mixed  $H_2/H_\infty$  design methodologies have been reported in [50.39, 40, 42]. A control design using mixed  $H_2/H_\infty$  for the MEMS microactuator dual-stage servo system will be presented in Sect. 50.3.3.

Other advanced control theories also have been applied to dual-stage servo control designs, such as sliding-mode control [50.43] and neural networks [50.44].

### 50.3.3 Servo Control and Vibration Attenuation of a MEMS Microactuator Dual-Stage Servo System with an Instrumented Suspension

#### System Modeling

MEMS microactuators for dual-stage servo applications are usually designed to have a single flexure resonance mode between approximately 1–3 kHz [50.45–47]. This resonance mode is usually lightly damped with a damping ratio of about 0.1, and hence the microactuator is susceptible to airflow turbulence and external disturbances. Capacitive sensing can be imbedded in MEMS microactuators to measure the position of the microactuator relative to the suspension tip [50.14, 45]. This relative position signal can be utilized to damp the microactuator's resonance mode in order to make a well-behaved microactuator and ease the control design that follows [50.48].

In addition to the use of dual-stage actuators for achieving higher servo bandwidth, instrumented suspensions have also been proposed as a means of providing information on airflow-excited suspension vibrations. The sensor output can be used for VCM–suspension mode damping to increase its bandwidth [50.30], or be used for feed-forward vibration compensation by the microactuator [50.49], or both [50.42].

The block diagram of a dual-stage system with a MEMS microactuator and an instrumented suspension is illustrated in Fig. 50.24. In the figure,  $G_V$  and  $G_M$  represents the VCM and microactuator dynamics respectively,  $w_v$  and  $w_m$  are airflow disturbances acting on the VCM and microactuator respectively,  $u_v$  and  $u_m$

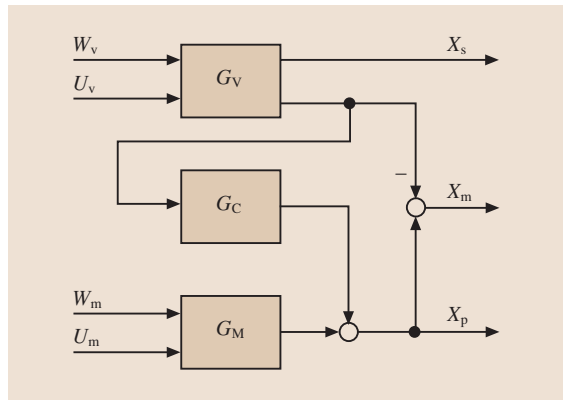


**Fig. 50.24** General plant for the dual-stage actuator with an instrumented suspension

are the control inputs.  $x_p$ ,  $x_s$ ,  $x_m$ , and  $x_v$  are respectively the read/write head position, the strain sensor output from the instrumented suspension, the relative motion output from the capacitive sensor embedded in the microactuator, and the suspension tip position.  $G_M$  can be modeled as a second-order system with the following transfer function

$$G_M(s) = \frac{A_m}{s^2 + 2\zeta_m\omega_m s + \omega_m^2}, \quad (50.17)$$

where  $A_m$ ,  $\omega_m$  and  $\zeta_m$  are the modal constant, natural frequency and damping ratio, respectively.  $G_C$  represents the coupling dynamics from  $x_v$  to  $x_p$ . If the microactuator is rotary,  $G_C$  is a constant of value 1, and  $x_m$  is solely the output of the microactuator driven by  $u_m$ , implying no coupling between the two actuators [32.13]. If the microactuator is translational, then  $G_C$  can be derived from the microactuator to be

$$G_C(s) = \frac{2\zeta_m\omega_m s + \omega_m^2}{s^2 + 2\zeta_m\omega_m s + \omega_m^2}. \quad (50.18)$$

This coupling effect implies that actuation of the VCM will excite the microactuator dynamics, and  $x_m$  then becomes the combined output of  $G_V$  and  $G_M$ . In both cases, rotary and translational, actuation of the microactuator can be assumed to have little effect on the VCM dynamics, given the fact that the inertia of the microactuator is very small compared to that of the VCM. This assumption implies that the transfer function from  $u_m$  to  $x_v$  can be neglected.

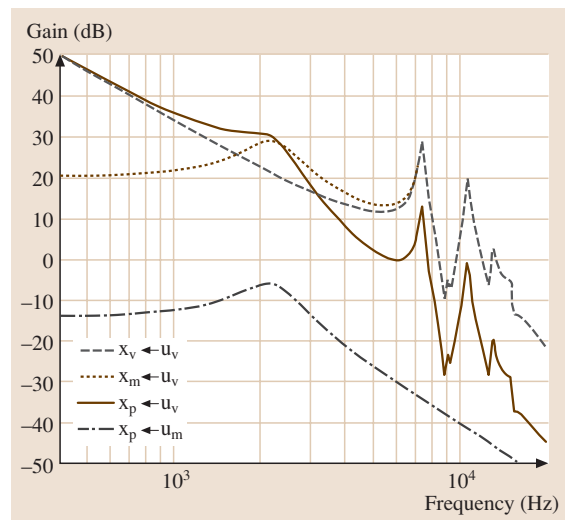


**Fig. 50.25** Frequency responses of the dual-stage plant

Figure 50.25 shows frequency responses of the dual-stage plant with a translational microactuator of the type described in Section 50.2.3. The VCM–suspension assembly has several suspension modes in the high-frequency range. The microactuator resonance mode is located at about 2.2 kHz. Due to the coupling effect  $G_C$ , the responses of  $x_p$  and  $x_v$  from  $u_v$  are different:  $x_v$  is filtered by  $G_C$  in the frequency range above the microactuator resonance mode. In the rotary microactuator case, the two responses are the same, and the response from  $u_v$  to  $x_m$  is always zero. This coupling/decoupling effect makes a difference between the rotary and translational microactuators. From the viewpoint of suspension vibration attenuation, we would like to have a soft spring and a light damping effect, such that most high-frequency suspension vibrations can be attenuated when passing through the microactuator. On the other hand, we want a stiff spring and heavy damping so that the response from  $u_v$  to  $x_p$  has high gains in a wide frequency range for effective track following by the VCM. A tradeoff is therefore necessary between high-frequency vibration attenuation and low-frequency track following, depending on the relative magnitude of runout, which is mainly in the low frequency range, versus suspension vibration, which is mainly in the high frequency range.

#### Minor-Loop Vibration Damping Design

When  $x_m$  and  $x_s$  are assumed to be available as auxiliary information, it is possible to first design minor-loop vibration damping controllers before designing an outer-loop tracking controller for the dual-stage servo system. In addition, the two signals can be sampled at a higher rate than that of the PES, which is determined by the hardware configuration, so as to achieve better control effects.

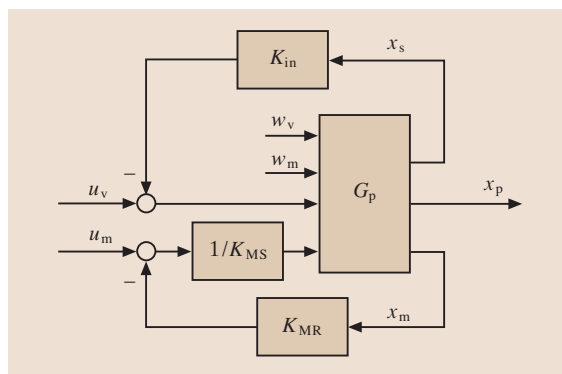


**Fig. 50.26** Minor-loop vibration damping and compensation

**Microactuator Resonance Mode Damping.** The basic use of the relative motion signal,  $x_m$ , is to actively damp the microactuator resonance mode to make for a well-behaved microactuator and to simplify the control design that follows. This can be implemented as a minor loop around the microactuator, as shown in the lower part of Fig. 50.26. Consider the discrete-time open-loop plant

$$G_M(q^{-1}) = \frac{q^{-1}B_0(q^{-1})}{A_0(q^{-1})}, \quad (50.19)$$

where  $q^{-1}$  is the one-step delay operator.  $B_0(q^{-1})$  is the plant zero polynomial, and  $A_0(q^{-1}) = 1 + a_1q^{-1} + a_2q^{-2}$  is the plant pole polynomial. The desired damped microactuator can be expressed as

$$G_{MD}(q^{-1}) = \frac{q^{-1}B_0(q^{-1})}{A_D(q^{-1})}. \quad (50.20)$$

With the controller structure shown in Fig. 50.26,  $G_{MD}$  can be achieved by solving the following Diophantine equation

$$A_D(q^{-1}) = A_0(q^{-1})K_{MS}(q^{-1}) + q^{-1}B_0(q^{-1})K_{MR}(q^{-1}). \quad (50.21)$$

The closed-loop polynomial  $A_D(q^{-1})$  is chosen by the designer. Usually the damping coefficient for  $G_{MD}$  is set to one, and the natural frequency  $\omega_{MR}$  can be replaced to achieve adequate gains in the low frequency range.

**Suspension Resonance Modes Damping.** After the minor loop around the microactuator is closed, a vibration controller  $K_{in}$  is designed using  $x_s$  to provide more damping of the suspension resonance modes. The design of  $K_{in}$  is formulated as a standard LQG problem. Consider the discrete-time representation of  $G_V$  as shown in Fig. 50.26:

$$\begin{aligned} x(k+1) &= Ax(k) + Bu_v(k) + B_w w_v(k), \\ y(k) &= Cx(k) + n(k), \end{aligned} \quad (50.22)$$

where  $y(k) = [x_v(k) \ x_s(k)]^T$ , and the airflow turbulence  $w_v(k)$  and measurement noise  $n(k)$  are random signals with zero mean. In this model for controller design, only two major suspension modes are included in order to restrain the controller order and to avoid high-frequency vibration spillover. The goal of designing  $K_{in}$  is to minimize the cost function

$$J = E \left\{ x_v^2(k) + Ru_v^2(k) \right\}, \quad (50.23)$$

where  $E\{\cdot\}$  is the expectation operator and  $R$  is a control weight.

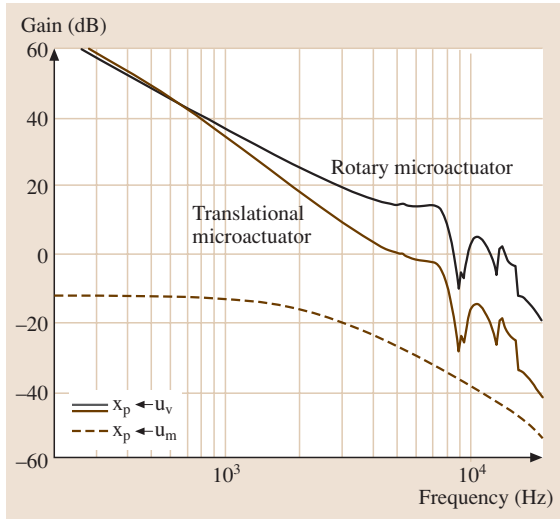


**Fig. 50.27** Frequency responses of the damped plant

Figure 50.27 shows the frequency responses of the two damped subsystems. Two major resonance modes of the VCM–suspension assembly and the microactuator mode have been damped using  $x_s$  and  $x_m$ , respectively. As can be seen, the frequency response from  $u_v$  to  $x_p$  for the translational microactuator case has stronger high-frequency attenuation than that for the rotary microactuator case due to the coupling effect. This implies that the translational microactuator will behave better in suspension vibration attenuation, which happens in the high frequency range.

**Track-Following Control Design Using the Sensitivity-Decoupling Method**

*Sensitivity-Decoupling Design Methodology.* The sensitivity-decoupling design approach, originally proposed in [50.36] and explored in detail in [50.13], is popularly applied in the design of track-following controllers for dual-stage systems. This approach utilizes the PES and  $y_m$  to estimate the position error of the suspension tip relative to the data track center, which is also called the VPES,

$$VPES = PES + x_m = r - x_v, \tag{50.24}$$

where  $r$  represents track runout. This configuration is illustrated in Fig. 50.28a, where  $G_{PD}$  is the damped plant, as shown in Fig. 50.26. It can be shown that, for the dual-stage system shown in Fig. 50.24, with a either rotary or translational microactuator, it is equivalent to the sensitivity block diagrams as shown in Fig. 50.28b and c, where  $G_{VD}$  and  $G_{MD}$  are the damped versions of  $G_V$

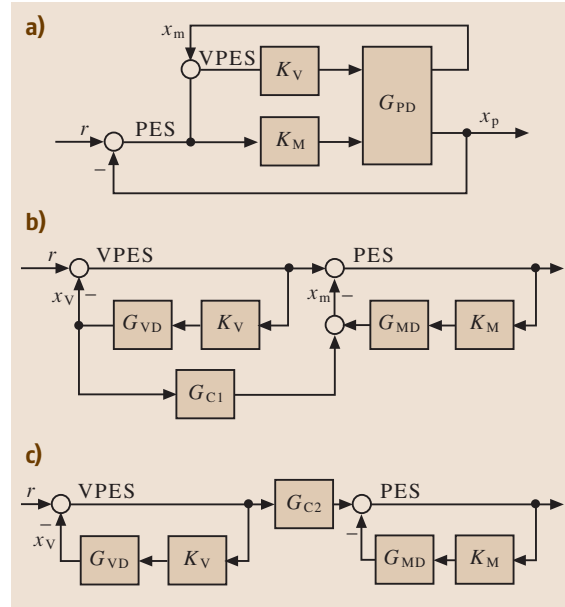


**Fig. 50.28** Sensitivity-decoupling design

and  $G_M$  respectively, and  $G_{C1}$  and  $G_{C2}$  are derived to be

$$G_{C1} = \frac{K_{MS}}{K_{MS} + G_M K_{MR}} (G_C - 1), \tag{50.25}$$

$$G_{C2} = 1 - G_{C1} G_V K_V. \tag{50.26}$$

The total closed-loop sensitivity from  $r$  to the PES can then be expressed as

$$S_T = S_V G_{C2} S_M, \tag{50.27}$$

where

$$S_V = \frac{1}{1 + K_V G_{VD}}, \quad S_M = \frac{1}{1 + K_M G_{MD}}. \tag{50.28}$$

With the configuration shown in Fig. 50.28c, decoupling the designs of  $K_V$  and  $K_M$  is made possible: the VCM loop and the microactuator loop can be designed sequentially using conventional SISO design techniques.

*Coupling Compensation for Translational Microactuators.* It is worthwhile to pay special attention to the coupling effect in this design process. The blocks,  $G_{C1}$  and  $G_{C2}$ , in Fig. 50.28 are derived from the coupling effect  $G_C$  shown in Fig. 50.24 and (50.18). As can be seen, for a rotary microactuator,  $G_C = 1$ , then  $G_{C1} = 0$  and  $G_{C2} = 1$ , implying exact decoupling between the

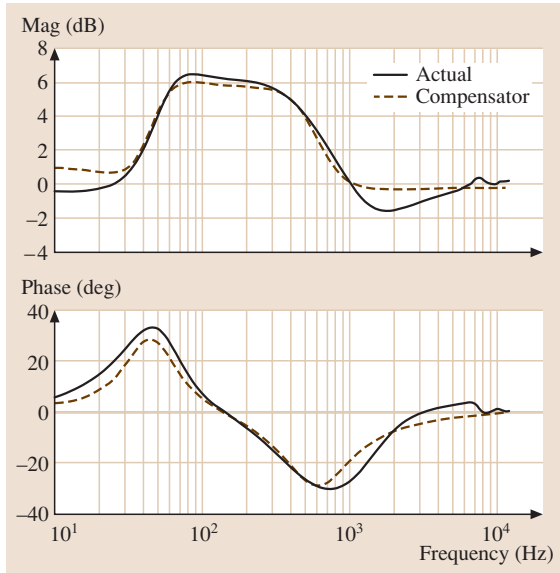


**Fig. 50.29** Frequency responses of  $G_{C2}$  and the compensator  $K_C$

two minor loops in Fig. 50.28c. In the translational microactuator case,  $G_{C2}$  involves all plant dynamics and designed controllers except for  $K_M$ . The frequency response of  $G_{C2}$  is shown in Fig. 50.29. It is seen that the dynamics of  $G_{C2}$  are fairly mild: it is about 6 dB in the region of 60–500 Hz, and close to 0 dB beyond 1 kHz. Its phase property is mild as well:  $30^\circ$  around 60 Hz and  $-30^\circ$  around 600 Hz. This implies that, based on the  $K_M$  designed for the rotary microactuator case, a modifier, which has similar dynamics to  $G_{C2}$ , can be designed to compensate for the coupling effect, yielding a sensitivity response similar to that of the rotary microactuator case:

$$K_{MC} = K_M K_C \approx K_M G_{C2}, \quad (50.29)$$

where  $K_M$  is the controller designed for the rotary microactuator case,  $K_C$  is a modifier to compensate for  $G_{C2}$ , and its dynamics are also shown in Fig. 50.29 in dashed lines.

**Dual-Stage Sensitivity-Function Design.** In the rotary microactuator case, the design of  $K_V$  and  $K_M$  is to use pole placement. The VCM loop sensitivity is designed to achieve enough attenuation in the low frequency range, to deal with large-amplitude disturbance components. The microactuator loop sensitivity is designed to expand the bandwidth and to achieve further attenuation of low-

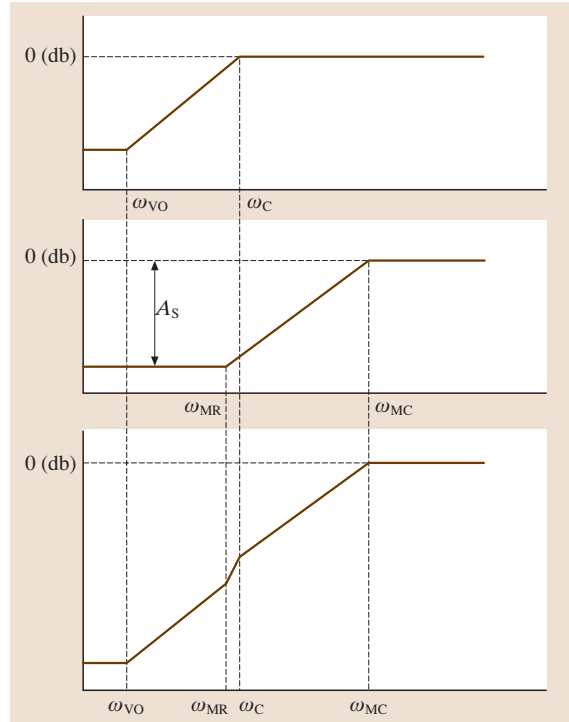


**Fig. 50.30** Illustration of dual-stage sensitivity  $S_T$  design

frequency runout and disturbances. The compensators in the dual-stage servo system depicted in Fig. 50.28 can be designed by a two-step design process, as illustrated in Fig. 50.30.

First, the VCM loop compensator,  $K_V$ , is designed to attain a desired VCM closed-loop sensitivity  $S_V$ , as shown in the top part of Fig. 50.30. Its bandwidth,  $\omega_{VC}$  in Fig. 50.30, is generally limited by the E-block and suspension resonance modes. The design of this compensator can be accomplished using conventional SISO frequency-shaping techniques.

The second step of the design process involves the design of the microactuator loop compensators to attain additional attenuation  $S_M$ , as shown in the middle part of Fig. 50.30. As mentioned in Sect. ??<sup>TS11</sup>, the minor loop compensator,  $K_{MR}/K_{MS}$ , is determined in order to damp the microactuator resonance mode and place the poles of  $G_{MD}$ , or equivalently  $\omega_{MR}$  in Fig. 50.30, at a desired location. The poles of  $G_{MD}$  will become the zeros of  $S_M$ .

Finally, the microactuator loop compensator,  $K_M$ , is designed to place the poles, or equivalently  $\omega_{MC}$  in Fig. 50.30, of the microactuator loop sensitivity  $S_M$ .

<sup>9</sup> The horizontal axes in this figure are unlabeled  
<sup>10</sup> Please check the symbol  $S_T$  in this caption  
<sup>11</sup> Which section do you mean?

$\omega_{MC}$  is limited by the PES sampling frequency and computational time delay [50.50].

The total dual-stage sensitivity is shown in the bottom part of Fig. 50.30. For a given  $\omega_{MC}$ , the additional attenuation  $A_S$ , provided by the microactuator loop, will be determined by  $\omega_{MR}$ . In our proposed procedure, the initial value of  $\omega_{MR}$  can be chosen to be the same as  $\omega_{VC}$ . It is then adjusted so that the desired attenuation and phase-margin requirements of the overall dual-stage system are satisfied. Decreasing  $\omega_{MR}$  increases the low-frequency attenuation of the closed-loop sensitivity function  $S_T$ , but also generally reduces the phase margin of open-loop transfer function  $G_T$ .

**Servo Design Using the Mixed  $H_2/H_\infty$  Design Approach.** In this section, a multi-objective optimization method, also called the mixed  $H_2/H_\infty$  approach, is applied to the design of tracking controllers [50.42]. Unlike the sensitivity-decoupling approach, which proceeds sequentially by using SISO design techniques, the mixed  $H_2/H_\infty$  approach is a MIMO design approach. It formulates the optimization of tracking performance as a  $H_2$  control problem, and stability robustness is explicitly considered by posing some  $H_\infty$  norm bounds. Figure 50.31 shows the schematic for this method.

In Fig. 50.31,  $G_{RO}$  is the frequency-shaping function for generating track runout from the normalized noise  $w_r$ .  $n_1$  and  $n_2$  are measurement noises.  $G_{in}$  is the damped plant model with the microactuator damping and  $K_{in}$  closed.  $\Delta := \text{diag}(\Delta_V, \Delta_M)$  represents multiplicative uncertainties of the nominal actuator model and will be explained later.

**Tracking-Following Error Minimization.** The main objective of the dual-stage servo system is to make the PES as small as possible, in order to achieve high areal density and low readout error rates. Since the whole system has been adequately modeled as a stochastic system, that is, all disturbances are modeled as random signals with Gaussian distributions, tracking performance is normally characterized by the  $3\text{-}\sigma$  value of the PES. When all those disturbances are normalized using corresponding weighting functions, minimizing the RMS value is then equivalent to minimizing the  $H_2$  norm of the following transfer function

$$\min \text{RMS (PES)} \Leftrightarrow \min \|G_{z_2 w_2}\|_2, \quad (50.30)$$

where  $z_2 = [\text{PES } u_v \ u_m]^T$  and  $w_2 = [w_r \ w_v \ w_m \ n_1 \ n_2]^T$ . This is just an  $H_2$  optimization problem.

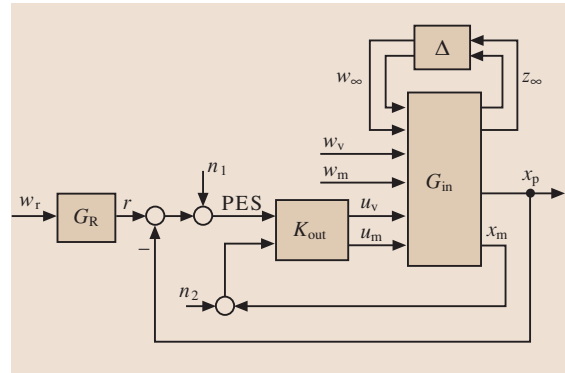


Fig. 50.31 Multi-objective optimization

**Stability Robustness Consideration.** Stability robustness is an important issue for practical implementation of hard-disk servo controllers, since there always exist uncertainties and variations in disk drives' plant dynamics. It is infeasible to fine-tune controller parameters for each individual disk drive and actual working situations. Therefore, the designed controller should retain stability over a large batch of drives. In other words, it should exhibit stability robustness to plant uncertainties and variations. To this end, both qualitative and quantitative information about plant uncertainties need to be obtained to some extent and be taken into consideration during the design process. In this design example, the plant uncertainty is modeled to be multiplicative uncertainty in the following form:

$$\begin{aligned} G_V(s) &= G_{Vnom}(s)[1 + \Delta_V(s)W_V(s)], \\ G_M(s) &= G_{Mnom}(s)[1 + \Delta_M(s)W_M(s)]. \end{aligned} \quad (50.31)$$

Here,  $G_{Vnom}$  and  $G_{Mnom}$  are the nominal dynamics of the VCM and microactuator, respectively.  $\Delta_V$  and  $\Delta_M$  have been scaled by the gain bounding functions  $W_V$  and  $W_M$  respectively, such that  $\|\Delta_V\|_\infty \leq 1$ ,  $\|\Delta_M\|_\infty \leq 1$ . Usually the bounding functions,  $W_V$  and  $W_M$ , have large magnitudes in the high frequency range, implying more uncertainty due to unmodeled dynamics and plant variation

$$\begin{aligned} W_V(s) &= \frac{3s^2 + 3 \times 10^4 s + 1.4 \times 10^8}{s^2 + 4.6 \times 10^4 s + 1.4 \times 10^9}, \\ W_M(s) &= \frac{s + 6.28 \times 10^3}{s + 6.28 \times 10^4}. \end{aligned} \quad (50.32)$$

To guarantee stability robustness of the closed-loop system, the following conditions should be satisfied [50.51],

$$\sup_{\omega} \mu_{\Delta} [G_{cl}(j\omega)] < 1, \quad (50.33)$$

where  $G_{cl}$  is the closed-loop system with  $K_{out}$  closed around  $G_{in}$ , and  $\mu$  is the structured singular value of  $G_{cl}$  with respect to the uncertainty  $\Delta$ . Since the dimension of the  $\Delta$  block is only 2 in this design, condition (50.33) can be approximated by setting  $\mu$ -bounds on the two uncertain channels individually, that is,  $\sup \mu_{\Delta_V}[G_{cl}(j\omega)] < \gamma_V$  and  $\sup \mu_{\Delta_M}[G_{cl}(j\omega)] < \gamma_M$ , with  $\gamma_V$  and  $\gamma_M$  strictly less than 1 and determined by trial and error. The two inequalities can be further reduced to  $\|G_{cl,\Delta_V}\|_\infty < \gamma_V$  and  $\|G_{cl,\Delta_M}\|_\infty < \gamma_M$  when  $\Delta_V$  and  $\Delta_M$  are scalars.

**Multi-objective Optimization through Linear Matrix Inequalities (LMIs).** From the above discussions, we have shown that the multi-objective optimization problem can be cast as an  $H_2$  minimization problem with some  $H_\infty$  bounds, i. e., to design an output dynamic feedback controller  $K_{out}$  such that

$$K_{out} = \arg \min_{K_{out}} \gamma_2, \quad (50.34)$$

$$\text{with } \|G_{z_2 w_2}\|_2 < \gamma_2, \quad (50.35)$$

$$\|G_{z_\infty w_\infty, \Delta_V}\|_\infty < \gamma_V, \quad (50.36)$$

$$\text{and } \|G_{z_\infty w_\infty, \Delta_M}\|_\infty < \gamma_M. \quad (50.37)$$

This minimization problem with inequalities can be transformed to a set of LMIs and be solved with a convex optimization algorithm, such as SeDuMi [50.52].

The designed controller,  $K_{out}$ , is a MIMO controller. Figure 50.31 shows the frequency response of  $K_{out}$  for the translational microactuator case, from the PES to  $w_v$ . We can see that there is a large peak for the  $H_2$  design, which implies the potential for poor stability robustness due to plant variation. When the  $H_\infty$  bounds are imposed, that peak is suppressed significantly in order to achieve more stability robustness.

#### Adaptive Feed-Forward Compensation for Suspension Vibration

As mentioned before, some suspension resonance modes can be damped by using the strain signal  $x_s$  measured from the suspension. Actually this signal can further be exploited to drive the microactuator to compensate for airflow-excited suspension vibrations appearing at  $x_p$  [50.13].

Define  $G_{ws}$  and  $G_{wp}$  to be the transfer functions from  $w_v$  to  $x_s$  and  $x_p$  respectively. We want the feed-forward compensator,  $K_{MF}$ , to minimize airflow-excited vibrations at the head, i. e., to minimize

$$e_a = G_M K_{MF} G_{ws} w_v + G_{wp} w_v. \quad (50.38)$$

This scheme is different from feedback damping of the VCM in that the motion generated by the microactuator cannot directly affect the suspension outputs,  $x_v$  and  $x_s$ . Instead, what it can do is to compensate for those vibrations at the head that result from suspension vibration. It is also desirable to tune the coefficients of  $K_{MF}$  in real time in order to take into account the following factors that are slowly time-varying: suspension dynamics variation from drive to drive, and the dependence of strain-sensor properties on ambient temperature and time.

In this design,  $K_{MF}$  assumes the form of a finite impulse response (FIR) for stability consideration:

$$K_{MF}(\theta, q^{-1}) = h_0 + h_1 q^{-1} + \dots + h_n q^{-n}, \quad (50.39)$$

where  $\theta$  is the filter coefficient vector  $\theta = [h_0 \ h_1 \ \dots \ h_n]^T$  and  $n$  is the order of  $K_{MF}$ . The feed-forward compensation motion can be expressed as

$$\begin{aligned} x_{MF}(k) &= G_M(q^{-1}) K_{MF}(q^{-1}) x_s(k) \\ &= K_{MF}(q^{-1}) G_M(q^{-1}) x_s(k) \\ &= K_{MF}(q^{-1}) x_f(k) \\ &= \theta^T \phi(k-1), \end{aligned} \quad (50.40)$$

where  $x_f(k) = G_M(q^{-1}) x_s(k)$ ,  $\phi(k) = [x_f(k) \ x_f(k-1) \ \dots \ x_f(k-n)]^T$ . Since  $x_f(k)$  is not directly measurable, it is estimated by passing  $x_s(k)$  through the model of the microactuator  $\hat{G}_M$ :

$$x_f(k) = \hat{G}_M(q^{-1}) x_s(k). \quad (50.41)$$

The coefficients of  $\theta$  is tuned in such a way that  $E\{e_a^2(k)\}$  is minimized. However,  $e_a$  is not directly measurable. What we have is the PES, and it can be expressed as

$$\text{PES}(k) = e_a(k) + e_r(k), \quad (50.42)$$

where  $e_r$  represents the tracking error resulting from all other disturbance sources except for the airflow turbulence acting on the suspension. It is roughly valid to assume that  $w_v$  and  $r$  are uncorrelated, then we have

$$E\{\text{PES}^2(k)\} = E\{e_a^2(k)\} + E\{e_r^2(k)\}. \quad (50.43)$$

Thus, minimizing  $E\{e_a^2(k)\}$  is equivalent to minimizing  $E\{\text{PES}^2(k)\}$ , and we can utilize the PES as a corrupted error signal to perform the adaptation. With  $e_a$  corrupted by  $e_r$ , there will be some degradation in feed-forward compensation performance, and a little longer time is needed for the adaptation process to converge.

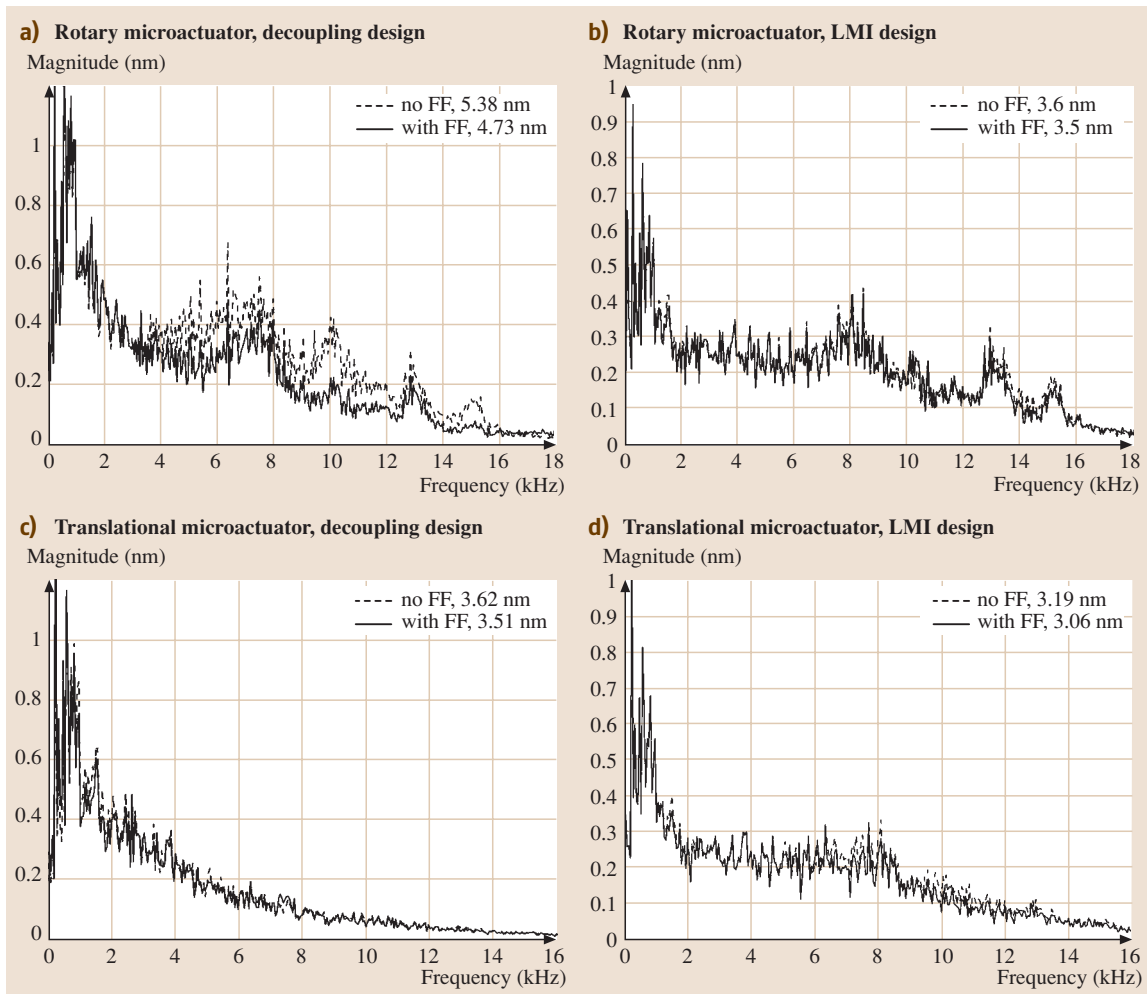


**Fig. 50.32a–d** Power spectra of the PES for various system configurations (a)Rotary microactuator, decoupling design (b)Rotary microactuator, LMI design (c)Translational microactuator, decoupling design (d)Translational microactuator, LMI design

### Simulation Results

Simulations are conducted to investigate the performance of systems with different structures and controllers. In the simulation, the reference signal  $r$  is generated from a combination of various sources, such as repeatable track runout, disk fluttering, low-frequency torque disturbances to the VCM, etc. Measurement noises are injected into the system at proper locations.

Figure 50.32 shows the simulation results for various configurations, in which FF means adaptive feed-forward compensation using  $x_s$ . Comparing (a) and (c), we can see significant differences between the rotary and translational microactuators, especially in the high

frequency range. There are almost no resonance modes showing up in (c) due to the coupling effect. Comparing (a) and (b), we see that the LMI design achieves better performance than the decoupling design by optimally shaping the sensitivity function and making a better balance between the attenuation of  $r$  and  $w_v$ . From (c) and (d), we can see more clearly the improvement achieved by optimal frequency shaping.

Table 50.2 summarizes the simulation results in more detail. In the table, the total PES has been decomposed into two parts:  $PES(w_v)$  and  $PES(r)$ , where  $PES(w_v) \equiv e_a$  and  $PES(r) \equiv e_r$ . After this decomposition, we can more clearly see the improvement by

**Table 50.2** Performance comparison between various plants and control designs

Plant type	Parameter variation	Tracking controller	PES( $r$ ) (nm)		PES( $w_v$ ) (nm)		Total PES (nm)	
			no FF	with FF	no FF	with FF	no FF	with FF
R <sup>CE-12</sup>	Nom	Decp	3.62	3.57	3.98	3.10 (22%)	5.38	4.73 (12%)
T	Nom. <sup>CE-13</sup>	Decp	3.49	3.51	0.96	0.65 (32%)	3.62	3.57 (2%)
R	Min.	LMI	2.75	2.73	2.75	2.53 (8%)	3.89	3.72 (5%)
R	Nom.	LMI	2.77	2.74	2.32	2.18 (6%)	3.61	3.50 (3%)
R	Max.	LMI	2.99	2.93	2.46	2.09 (15%)	3.87	3.60 (7%)
T	Min.	LMI	2.81	2.82	1.90	1.40 (26%)	3.39	3.15 (7%)
T	Nom.	LMI	2.78	2.78	1.56	1.28 (18%)	3.19	3.06 (4%)
T	Max.	LMI	2.81	2.79	1.67	1.35 (19%)	3.27	3.10 (5%)

**Table 50.3** Parameter variations of plant resonance modes

Parameters	Variations		
	Min.	Nom.	Max.
Suspension natural frequencies ( $\omega_i$ )	-10%	0	+10%
Microactuator natural frequency ( $\omega_m$ )	-15%	0	+15%
Damping coefficient ( $\zeta_i, \zeta_m$ )	-20%	0	+20%
Modal constants ( $A_i, A_m$ )	-5%	0	+5%

adaptive feed-forward compensation. In the table, R and T denote the rotary and translational plant cases, respectively. Two aforementioned design methods are employed: sensitivity-decoupling design and the LMI design. For plant parameter variation, three plant situations are considered: minimum, nominal and maximum. They indicate how much the plant's modal parameters vary, as specified in Table 50.3. In Table 50.2, those percentage numbers indicate how much improvement that is achieved by adaptive feed-forward compensation compared to the cases without FF as shown in the left columns.

Several conclusions can be drawn from Table 50.2.

1. The translational microactuator case always performs better than the rotary microactuator case in the attenuation of airflow-excited suspension vibrations, no matter what kind of design approach is used. We also see that the improvement is mainly achieved by reducing PES( $w_v$ ). Obviously this is due to the coupling/filtering effect of the translational microactuator on suspension vibration.
2. The LMI design achieves better performance than the decoupling design by better balancing the attenuation of PES( $r$ ) and PES( $w_v$ ). For the R-N case<sup>CE-14</sup>,

both PES( $r$ ) and PES( $w_v$ ) are reduced by the LMI design, while for the T-N case, the LMI design reduces PES( $r$ ) significantly by amplifying PES( $w_v$ ) a little, yielding a smaller total PES. This trend can also be seen from Fig. 50.32.

3. Adaptive feed-forward compensation can further attenuate PES( $w_v$ ), especially when there is plant variation. In practical implementation, the strain sensor may pick up some resonance modes that do not contribute to head offtrack motion. These modes are called non-offtrack modes and appear as measurement noise in feed-forward compensation. Optimization in sensor placement and orientation is therefore necessary to improve the signal-to-noise ratio (SNR) for better vibration compensation [50.32].
4. A combination of the LMI design and adaptive feed-forward compensation can achieve the best performance with fairly good performance robustness. For the rotary microactuator case, performance degradation under plant variation is less than 6%, while the degradation is less than 3% for the translational microactuator case. Again, the translational microactuator case achieves better performance robustness partially due to the coupling/filtering effect, which is very robust to parameter variations.

### 50.3.4 Multi-Rate Robust Track-Following Control: A Direct Approach

The controller design procedure in the previous section consists of three steps: fast-rate minor-loop damping controller design, down-sampling, and slow-rate outer-loop track-following controller design. In other words, controllers with different sampling rates have been designed separately. In contrast, in this section, we will present a robust control technique which directly designs a multi-rate controller. The model under consideration

<sup>CE-12</sup> Please define the following abbreviations in this table: R, T, Decp  
<sup>CE-13</sup> Consider clarifying the meaning of the terms Min, Max and Nom in this figure  
<sup>CE-14</sup> Please clarify what R-N and T-N mean in this paragraph

in this section is the same as the one explained in Sect. 50.3.3.

### Design Procedure for Multi-Rate Controllers

A multi-rate robust track-following problem is formulated as follows. Design a discrete-time controller  $K$  which has two outputs  $(u_v, u_m)$  and three inputs (PES,  $y_s, y_m$ ), where  $y_s := x_s + n_3$  and  $y_m := x_m + n_2$  are noise-corrupted signals, such that the PES has a small RMS value, and that the closed-loop system is robustly stable for uncertainties  $\Delta_V$  and  $\Delta_M$ , as well as parametric uncertainties in  $G_V$  and  $G_M$ . Next, we shall provide a procedure to design a controller which solves this problem.

### A Generalized Plant

First, we construct a continuous-time generalized plant, which reflects the robust track-following problem, as depicted in Fig. 50.33, by extracting the uncertainties and by connecting a discrete-time controller  $K$  with a multi-rate sampler  $S$  and a zero-order hold  $H$ . We discretize the generalized plant by using the zeroth-order hold with a sampling rate of 50 kHz.

Although our main goal is to obtain a small PES, we have included  $(u_v, u_m)$  in the controlled output channel, to impose constraints on input magnitudes.

### Derivation of a Periodically Time-Varying System

Next, following the technique used in [50.?] <sup>TS15</sup>, the multi-rate sampler  $S$  can be written mathematically as  $S: \tilde{y}(k) = \Gamma(k)y(k), k = 0, 1, 2, \dots$ , where  $\{\Gamma(k)\}_{k \geq 0}$  is a sequence of matrices defined by <sup>CE16</sup>

$$\left\{ \Gamma(k) := \begin{cases} I_3, & \text{if } k \text{ is even} \\ \begin{pmatrix} 0 & 0 \\ 0 & I_2 \end{pmatrix}, & \text{if } k \text{ is odd} \end{cases} \right\}_{k \geq 0}. \quad (50.44)$$

The sequence  $\{\Gamma(k)\}_{k \geq 0}$  captures the multi-rate nature of our problem; at even times, we sample all the measurements, while at odd times, we cannot measure PES because of its slow sampling rate. Similarly, we can express the hold  $H$  as  $H: u(k) = \tilde{u}(k)$ , for  $k = 0, 1, 2, \dots$ . This means that we send both control signals at the fast sampling rate of 50 kHz, in order to achieve high track-following performance of the closed-loop system.

Combining the sampler  $S$  and the hold  $H$  with the discretized generalized plant results in the following periodically time-varying generalized plant. In our case, this plant is periodically time-varying with period 2.

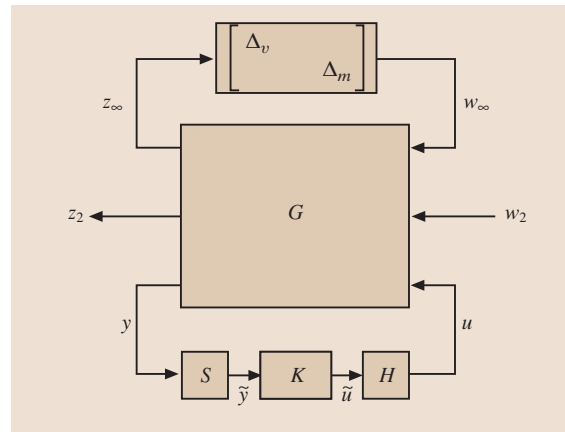


**Fig. 50.33** A generalized plant  $G$  with an uncertainty block and a multi-rate controller

### A Mixed $H_2/H_\infty$ Control Problem for the Periodically Time-Varying System

Using the generalized plant  $G$ , we formulate an optimization problem which reflects our control problem as follows:

$$\min_K \gamma_0 \text{ subject to } \begin{cases} K \text{ stabilizes the nominal system,} \\ |T_{z_2 w_2}|_2 < \gamma_0 \\ |e_i^T T_{z_\infty w_\infty} e_i| < \gamma_i, \quad i = 1, 2, \end{cases} \quad (50.45)$$

where  $T_{qp}$  denotes the map from the channel  $p$  to the channel  $q$ ,  $e_i$  is the  $i$ -th unit vector, and  $\gamma_i$  is a positive scalar to be tuned by the designer.

We remark that the norms used in (50.45) are for time-varying systems. The norm  $|\cdot|_2$  is a generalization of the standard  $H_2$  norm to a norm for time-varying systems, and is defined in [50.53]. On the other hand, the norm  $|\cdot|$  in (50.45) is used with an abuse of notation; it means the  $\ell_2$ -induced norm. We use this notation to emphasize that this optimization is a generalization of the standard mixed  $H_2/H_\infty$  optimization for time-invariant cases to that for time-varying cases. Roughly speaking, the minimization of  $|T_{z_2 w_2}|_2$  corresponds to the minimization of the RMS value of the PES, while the norm constraints on  $|e_i^T T_{z_\infty w_\infty} e_i|_\infty$  lead to robust stability against plant uncertainties  $\Delta_V$  and  $\Delta_M$ .

Results in [50.53–55] showed that many important control synthesis problems for time-varying systems can be solved in a very similar way to those for time-invariant systems. Moreover, for periodically time-varying systems, these problems can be reduced to finite-dimensional convex optimization problems,

<sup>TS15</sup> Please give cite.  
<sup>CE16</sup> Please confirm brackets in this equation

which can be solved by using linear matrix inequalities (LMIs). The designed controller becomes periodically time-varying with the same period as the original time-varying system.

### Simulation Results

The order of the designed periodically time-varying controller was 13. To evaluate the effectiveness of the multi-rate controller, we have also designed a single-rate controller, in which all output signals are sampled with the same 25 kHz rate as the PES. For comparison, we have set the same robust stability constraints,  $\gamma_1, \gamma_2$  in (50.45), during both the multi-rate and single-rate designs. For the single-rate case, the controller is time-invariant, and the order of the controller is also 13.

First, time domain simulations have been done for both controllers. The PES signals are shown in Fig. 50.34, where we can notice that the multi-rate controller achieves a smaller RMS value than its single-rate counterpart. This is also confirmed by the PES RMS values shown in Table 50.4. As can be seen in both the figures and the table, the track-following property can be greatly (about 30%) improved by using the multi-rate controller, with the same guaranteed robust stability margin. This illustrates the efficiency of the multi-rate controller for track-following.

Next, we test the robustness of the controllers. We have randomly generated, 1000 times, parameter variations within the ranges in Table 50.4, and checked how many times the multi-rate mixed  $H_2/H_\infty$  controller and the multi-rate  $H_2$  (LQG) controller stabilize the closed-loop system. A simulation result is shown in Table 50.5, where one can see that the multi-rate mixed  $H_2/H_\infty$  con-

**Table 50.4** Comparison of RMS values of the PES for the multi-rate and the single-rate controllers

		RMS of PES (nm)
Mixed $H_2/H_\infty$	Multi-rate	4.414
	Single-rate	6.274
LQG	Multi-rate	1.3659
	Single-rate	2.1958

**Table 50.5** Robustness test

Controller	Number of stabilized cases
Mixed $H_2/H_\infty$	956/1000
LQG	648/1000

troller is significantly more robust than the multi-rate LQG controller.

### 50.3.5 Dual-Stage Seek Control Design

Because the inertia of a microactuator is much smaller than that of the VCM, it can produce a larger acceleration and move faster than the VCM. The motion range of a microactuator is usually limited to a few micrometers, however. Thus the performance improvement in seek control made possible by using dual-stage actuation will mainly be in short-distance seeks.

Two-degree-of-freedom (2-DOF) position control has been a very popular control technique in short-distance seeks. A 2-DOF control technique utilizing decoupled feed-forward reference trajectories has been developed for short-span seek control using a PZT-actuated suspension dual-stage servo system [50.56].

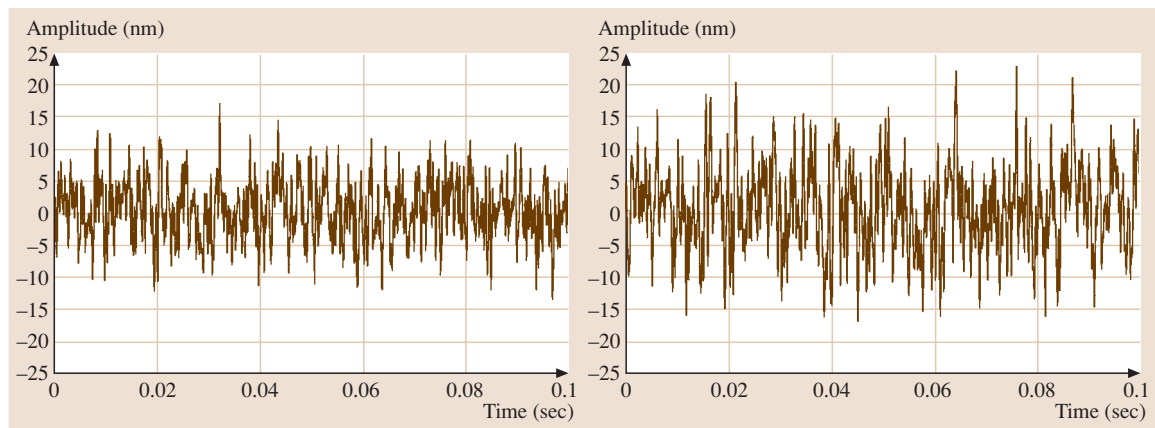


**Fig. 50.34** The position error signals for the multi-rate controller (*left figure*) and for the single-rate controller (*right figure*)

The same technique can also be applied to seek control of MEMS microactuator dual-stage servo systems.

Figure 50.35 shows a block diagram for dual-stage short-span seek control design using this method. In the figure,  $x_V^d$  and  $x_R^d$  are the desired seek trajectories of the VCM and the microactuator respectively.  $K_{VF}$  and  $K_{RF}$  are zero-phase-error tracking feed-forward controllers (ZPETFFC) generated using the VCM model  $G_V$  and the damped microactuator model  $G_R$  [50.57].

To minimize the residual vibration after a seek operation, minimum-jerk seek trajectories were applied to both the VCM and the microactuator. These can be generated by [50.58]

$$x_V^d(t) = 60 d_s \left[ \frac{1}{10} \left( \frac{t}{T_V} \right)^5 - \frac{1}{4} \left( \frac{t}{T_V} \right)^4 + \frac{1}{6} \left( \frac{t}{T_V} \right)^3 \right], \tag{50.46}$$

$$x_R^d = \begin{cases} 60 (d_s - x_V^d(T)) \times \left[ \frac{1}{10} \left( \frac{t}{T} \right)^5 - \frac{1}{4} \left( \frac{t}{T} \right)^4 + \frac{1}{6} \left( \frac{t}{T} \right)^3 \right] & t \leq T, \\ d_s - x_V^d(t) & t > T \end{cases} \tag{50.47}$$

where  $d_s$  is the distance of the head from the target track,  $T$  is the time when the head reaches the target track if dual-stage actuator is used, while  $T_V$  is the time when the head reaches the target track if only VCM is

used.  $T_V$  and  $T$  can be chosen based on the control force saturation and seek performance requirements.

Figure 50.36 shows the 1  $\mu\text{m}$  seek responses of the dual-stage actuator for the MIMO design. Overshoot was

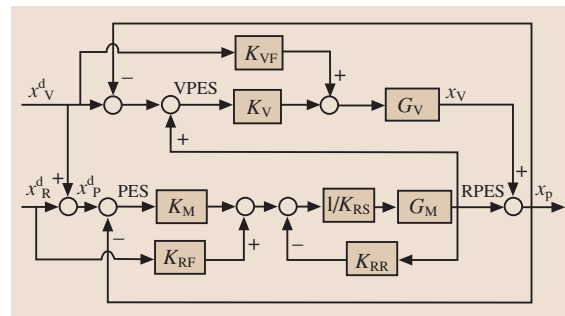


Fig. 50.35 Dual-stage seek control design

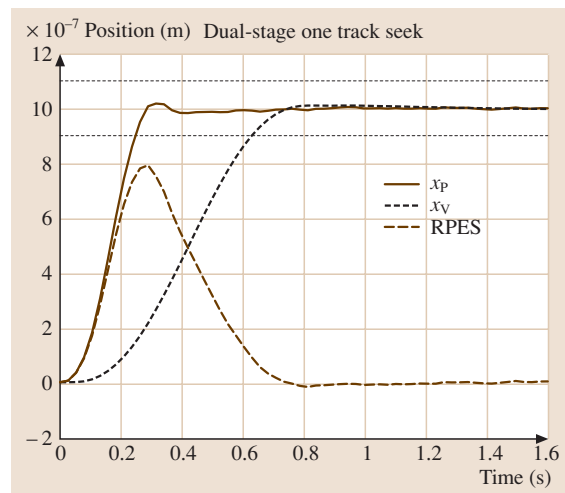


Fig. 50.36 Dual-stage short-span seek response

eliminated, and no obvious residual vibrations occurred. The seek time using the dual-stage actuator is about 0.25 ms, compared to a seek time of about 0.7 ms if only the VCM is used.

## 50.4 Conclusions and Outlook

In order to increase hard-disk-drive storage density, high-bandwidth dual-stage servo systems are necessary to suppress disturbances and increase servo precision. Various prototype MEMS microactuators have been designed and fabricated to provide a dual-stage actuation system. The most common approach for these prototypes is to use electrostatic driving arrays produced by MEMS fabrication methods.

MEMS microactuators provide a potentially high-performance and low-cost solution for achieving the servo requirements for extremely high HDD storage

density. Simulations and experiments show that many MEMS microactuator features, such as integrated silicon gimbals and capacitive relative-position-sensing arrays, can meet important requirements for operation of HDDs. The use of structural electrical isolation in the microactuator design could considerably reduce microactuator driving voltages, while processes that avoid the use of silicon-on-insulator wafers or high-temperature processing steps could reduce manufacturing costs. High-bandwidth dual-stage track-following controllers have been designed using both a decoupled SISO design

method and a variety of robust design methods, among others. In addition, short-span seeking control using a 2-DOF control structure with decoupled feed-forward trajectory generation can greatly reduce the short-span seek time.

Research remains to be done in the areas of system integration, reliability, and performance enhancement for this technology to be utilized in commercial products. Cost and reliability are probably the most important obstacles to commercial implementation of actuated-slider dual-stage servo systems at this time. Streamlining of microactuator fabrication processes or development of a process compatible with that of the slider and head fabrication could reduce manufacturing costs, which are not quite yet economical. Meanwhile, dynamic behavior and reliability of the microactuator under disturbances from airflow, head-disk interaction, and particle presence are being studied experimentally by industry.

Further in the future, to achieve nanometer servo precision, third-generation dual-stage servo systems will have to employ an actuated head approach. Research in this area has just started, with the key problem being how to combine microactuator fabrication with read/write head fabrication. Another area of research is the use of MEMS technology to incorporate additional sensors, such as accelerometers and strain-gage vibration sensors, to suppress the TMR due to airflow and

external disturbances excited structural vibrations<sup>CE17</sup>. New robust, adaptive MIMO control architectures and algorithms must be developed for such a multisensing multiactuation servo system.

Besides the application of MEMS microactuators in dual-stage servo control of traditional rotating media magnetic HDDs, recent advances in MEMS and nanotechnology have made possible the development of a new class of miniaturized ultra-high-density storage devices that use probe arrays for recording and reading data. This new architecture abandons the traditional rotating media and flying-slider paradigm in favor of parallel  $x$ - $y$  scanning of entire probe arrays over a storage medium. The probe arrays and/or the media are moved with electrostatic or electromagnetic microactuators that generate  $x$ - $y$  in-plane relative motion, as well as  $z$ -axis out-of-plane relative motion. One example of this new generation of storage devices is IBM's *millipede*, which utilizes atomic force microscopy (AFM) recording technology [50.59]. Data is recorded on a polymer media by tiny depressions melted by a thermomechanical process by the AFM tips. 400 Gb/in<sup>2</sup> bit patterns have been demonstrated using thermal probes.

By any of the paths above, MEMS and nanotechnology will become a basic enabling technology for the development of future data storage devices, offering the capabilities of small size, low power consumption, ultra-high densities, low cost, and high performance.

## References

- 50.1 T. Yamaguchi: Modelling and control of a disk file head-positioning system, Proc. Inst. Mech. Eng. I (J. Syst. Cont. Eng.) **215**, 549–567 (2001)
- 50.2 T. Howell, R. Ehrlich, M. Lippman: TPI growth is key to delaying superparamagnetism's arrival, Data Stor. <sup>TS18</sup>, 21–30 (1999)
- 50.3 R. B. Evans, J. S. Griesbach, W. C. Messner: Piezoelectric microactuator for dual-stage control, IEEE Trans. Magn. **35**, 977–981 (1999)
- 50.4 I. Naniwa, S. Nakamura, S. Saegusa, K. Sato: Low voltage driven piggy-back actuator of hard disk drives, IEEE International MEMS 99 Conference, Orlando 1999, ed. by <sup>TS19</sup> (IEEE, Piscataway 1999) 49–52
- 50.5 D. Horsley: Microfabricated Electrostatic Actuators for Magnetic Disk Drives. Ph.D. Thesis (University of California, Berkeley 1998)
- 50.6 L. Muller: Gimballed Electrostatic Microactuators with Embedded Interconnects. Ph.D. Thesis (University of California, Berkeley 2000)
- 50.7 S. Koganezawa, K. Takaishi, Y. Mizoshita, Y. Uematsu, T. Yamada: Development of integrated piggyback milli-actuator for high density magnetic recording, International Conference on Micromechanics for Information and Precision Equipment 1997, ed. by <sup>TS19</sup> (IEEE, New York 1997) 20–23
- 50.8 L.-S. Fan, T. Hirano, J. Hong, P. R. Webb, W. H. Juan, W. Y. Lee, S. Chan, T. Semba, W. Imaino, T. S. Pan, S. Pattanaik, F. C. Lee, I. McFadyen, S. Arya, R. Wood: Electrostatic microactuator and design considerations for HDD application, IEEE Trans. Magn. **35**, 1000–1005 (1999)
- 50.9 T. Imamura, M. Katayama, Y. Ikegawa, T. Ohwe, R. Koishi, T. Koshikawa: MEMS-based integrated head/actuator/slider for hard disk drives, IEEE/ASME Trans. Mechatron. **3**, 166–174 (1998)

- 50.10 T. Imamura, T. Koshikawa, M. Katayama: Transverse mode electrostatic microactuator for MEM-based HDD slider, Proc. IEEE MEMS Workshop, San Diego 1996, ed. by [TS19](#) (IEEE, New York 1996) 216–221
- 50.11 S. Nakamura, K. Suzuki, M. Ataka, H. Fujita: An electrostatic micro actuator for a magnetic head tracking system of hard disk drives, Transducers '97, ed. by [TS19](#) (IEEE, Piscataway 1997) 1081–1084
- 50.12 Y. Soeno, S. Ichikawa, T. Tsuna, Y. Sato, I. Sato: Piezoelectric piggy-back microactuator for hard disk drive, IEEE Trans. Magn. **35**, 983–987 (1999)
- 50.13 Y. Li, R. Horowitz: Mechatronics of electrostatic microactuator for computer disk drive dual-stage servo systems, IEEE/ASME Trans. Mechatron. **6**, 111–121 (2001)
- 50.14 N. Wongkomet: Position Sensing for Electrostatic Micropositioners. Ph.D. Thesis (University of California, Berkeley 1998)
- 50.15 A. Hac, L. Liu: Sensor and actuator location in motion control of flexible structures, J. Sound Vib. **167**, 239–261 (1993)
- 50.16 K. Hiramoto, H. Doki, G. Obinata: Optimal sensor/actuator placement for active vibration control using explicit solution of algebraic Riccati equation, J. Sound Vib. **229**, 1057–1075 (2000)
- 50.17 C. K. Lee: Theory of laminated piezoelectric plates for the design of distributed sensors/actuators. Part I: Governing equations and reciprocal relationships, J. Acoustic Soc. Am. **87**, 1144–1158 (1990)
- 50.18 C. K. Lee, F. C. Moon: Modal sensors/actuators, ASME, J. Appl. Mech. **57**, 434–441 (1990)
- 50.19 P. Cheung, R. Horowitz, R. Howe: Design, fabrication and control of an electrostatically driven polysilicon microactuator, IEEE Trans. Magn. **32**, 122–128 (1996)
- 50.20 T. Chen, Y. Li, K. Oldham, R. Horowitz: MEMS application in computer disk drive dual-stage servo systems, J. Soc. Instrum. Control Eng. **41**, 412–420 (2002)
- 50.21 T.-L. Chen: Design and Fabrication of PZT-Actuated Silicon Suspensions for Hard Disk Drives. Ph.D. Thesis (University of California, Berkeley 2001)
- 50.22 C. G. Keller, R. T. Howe: HexSil tweezers for tele-operated micro-assembly, 10th Intl Workshop on Micro Electro Mechanical Systems (MEMS'97), Nagoya 1997, ed. by [TS19](#) (IEEE, New York 1997) 72–77
- 50.23 T. J. Brosnihan, J. M. Bustillo, A. P. Pisano, R. T. Howe: Embedded interconnect and electrical isolation for high-aspect-ratio, SOI inertial instruments, International Conference on Solid-State Sensors and Actuators, New York 1997, ed. by [TS19](#) (IEEE, New York 1997) 637–640
- 50.24 T. Hirano, L.-S. Fan, T. Semba, W. Y. Lee, J. Hong, S. Pattanaik, P. Webb, W.-H. Juan, S. Chan: Microactuator for tera-storage, IEEE Intl MEMS 1999 Conference, Orlando 1999, ed. by [TS19](#) (IEEE, Piscataway 1999) 6441–6446
- 50.25 T. Hirano, L.-S. Fan, T. Semba, W. Lee, J. Hong, S. Pattanaik, P. Webb, W.-H. Juan, S. Chan: High-bandwidth HDD tracking servo by a moving-slider micro-actuator, IEEE Trans. Magn. **35**, 3670–3672 (1999)
- 50.26 M. White, T. Hirano, H. Yang, K. Scott, S. Pattanaik, F. Y. Huang: High-bandwidth hard disk drive tracking using a moving-slider MEMS microactuator, 8th IEEE Int. Wkshop. Motion Control [TS18](#), 299–304 (2004)
- 50.27 T. Iizuka, T. Oba, H. Fugita: Electrostatic micro actuators with high-aspect-ratio driving gap for hard disk drive applications, Intl Symposium on micro-mechatronics and human science, ed. by [TS19](#) (IEEE, Piscataway 2000) 229–236
- 50.28 H. Kuwajima, K. Matsuoka: Thin film piezoelectric dual-stage actuator for HDD, InterMag Europe, Session BS04, ed. by [TS19](#) (IEEE, Piscataway 2000) BS4
- 50.29 Y. Lou, P. Gao, B. Qin, G. Guo, E.-H. Ong, A. Takada, K. Okada: Dual-stage servo with on-slider PZT microactuator for hard disk drives, InterMag Europe, Session BS03, Amsterdam 2002, ed. by [TS19](#) (IEEE, Piscataway 2002)
- 50.30 Y. Huang, M. Banthur, P. Mathur, W. Messner: Design and analysis of a high bandwidth disk drive servo system using an instrumented suspension, IEEE/ASME Trans. Mech. **4**, 196–206 (1999)
- 50.31 F. Y. Huang, T. Semba, W. Imano, F. Lee: Active damping in HDD actuator, IEEE Trans. Mag. **37**, 847–849 (2001)
- 50.32 K. Oldham, S. Kon, R. Horowitz: Fabrication and optimal strain sensor placement on an instrumented disk drive suspension for vibration suppression, Proc. 2004 Am. Control Conf. [TS18](#), 1855–1861 (2004)
- 50.33 H. Fujita, K. Suzuki, M. Ataka, S. Nakamura: A microactuator for head positioning system of hard disk drives, IEEE Trans. Magn. **35**, 1006–1010 (1999)
- 50.34 B.-H. Kim, K. Chun: Fabrication of an electrostatic track-following micro actuator for hard disk drives using SOI wafer, J. Micromech. Microeng. **11**, 1–6 (2001)
- 50.35 R. Ehrlich, D. Curran: Major HDD TMR sources, and projected scaling with TPI, IEEE Trans. Magn. **35**, 885–891 (1999)
- 50.36 K. Mori, T. Munemoto, H. Otsuki, Y. Yamaguchi, K. Akagi: A dual-stage magnetic disk drive actuator using a piezoelectric device for a high track density, IEEE Trans. Magn. **27**, 5298–5300 (1991)
- 50.37 S. J. Schroeck, W. C. Messner, R. J. McNab: On compensator design for linear time-invariant dual-input single-output systems, IEEE/ASME Trans. Mechatron. **6**, 50–57 (2001)
- 50.38 T. Semba, T. Hirano, L.-S. Fan: Dual-stage servo controller for HDD using MEMS actuator, IEEE Trans. Magn. **35**, 2271–2273 (1999)

- 50.39 T. Suzuki, T. Usui, M. Sasaki, F. Fujisawa, T. Yoshida, H. Hirai: Comparison of robust track-following control systems for a dual stage hard disk drive, Proc. of International Conference on Micromechanics for Information and Precision Equipment, ed. by B. Bhushan, K. Ohno (Word Scientific, Singapore 1997) 101–118
- 50.40 X. Hu, W. Guo, T. Huang, B. M. Chen: Discrete time LQG/LTR dual-stage controller design and implementation for high track density HDDs, Proc. of American Automatic Control Conference, ed. by <sup>TS19</sup> (IEEE, Piscataway 1999) 4111–4115
- 50.41 S.-M. Suh, C. C. Chung, S.-H. Lee: Design and analysis of dual-stage servo system for high track density HDDs, *Microsyst. Technol.* **8**, 161–168 (2002)
- 50.42 X. Huang, R. Nagamune, R. Horowitz, Y. Li: Design and analysis of a dual-stage disk drive servo system using an instrumented suspension, Proc. Am. Control Conf. <sup>TS18</sup>, 535–540 (2004)
- 50.43 S.-H. Lee, S.-E. Baek, Y.-H. Kim: Design of a dual-stage actuator control system with discrete-time sliding mode for hard disk drives, Proc. of the 39th IEEE Conference on Decision and Control, ed. by <sup>TS19</sup> (IEEE, Piscataway 2000) 3120–3125
- 50.44 M. Sasaki, T. Suzuki, E. Ida, F. Fujisawa, M. Kobayashi, H. Hirai: Track-following control of a dual-stage hard disk drive using a neuro-control system, *Eng. Appl. Artif. Intell.* **11**, 707–716 (1998)
- 50.45 D. Horsley, N. Wongkomet, R. Horowitz, A. Pisano: Precision positioning using a microfabricated electrostatic actuator, *IEEE Trans. Magn.* **35**, 993–999 (1999)
- 50.46 L. S. Fan, T. Hirano, J. Hong, P. R. Webb, W. H. Juan, W. Y. Lee, S. Chan, T. Semba, W. Imaino, T. S. Pan, S. Pattanaik, F. C. Lee, I. McFadyen, S. Arya, R. Wood: Electrostatic microactuator and design considerations for hdd application, *IEEE Tran. Mag.* **35**, 1000–1005 (1999)
- 50.47 K. Oldham, X. Huang, R. Horowitz: Design, fabrication, and control of a high-aspect ratio microactuator for vibration suppression in a hard disk drive, Proc. 16th IFAC World Congress <sup>TS18</sup> (2005)tbp
- 50.48 M. T. White, T. Hirano: Use of relative position signal for microactuators in hard disk drives, Proc. Am. Control Conf. <sup>TS18</sup>, 2335–2540 (2003)
- 50.49 Y. Li, F. Marcassa, R. Horowitz, R. Oboe, R. Evans: Track-following control with active vibration damping of a PZT-actuated suspension dual-stage servo system, Proc. Am. Control Conf. <sup>TS18</sup>, 2553–2559 (2003)
- 50.50 M. T. White, W. M. Lu: Hard disk drive bandwidth limitations due to sampling frequency and computational delay, Proc. 1999 IEEE/ASME Int. Conf. Intelligent Mechatronics <sup>TS18</sup>, 120–125 (1999)
- 50.51 G. J. Balas, J. C. Doyle, K. Glover, A. Packard, R. Smith:  *$\mu$ -Analysis and Synthesis Toolbox* (MUSYN Inc. and The MathWorks, Natick 1995)
- 50.52 J. F. Sturm: Using Sedumi 1.05, A MATLAB Toolbox for Optimization over Symmetric Cones, <http://fewcal.kub.nl/sturm/software/sedumi.html> (2001)
- 50.53 M. A. Peters, P. A. Iglesias: *Minimum Entropy Control for Time-Varying Systems* (Birkhäuser <sup>CE20</sup>, 1997)
- 50.54 G. E. Dullerud, S. Lall: A new approach for analysis and synthesis of time-varying systems, *IEEE Trans. Automatic Control* **44**, 1486–1497 (1999)
- 50.55 S. Lall, G. Dullerud: An LMI solution to the robust synthesis problem for multi-rate sampled-data systems, *Automatica* **37**, 1909–1922 (2001)
- 50.56 M. Kobayashi, R. Horowitz: Track seek control for hard disk dual-stage servo systems, *IEEE Trans. Magn.* **37**, 949–954 (2001)
- 50.57 M. Tomizuka: Zero phase error tracking algorithm for digital control, *Trans. ASME J. Dynam. Syst. Meas. Control* **109**, 65–68 (1987)
- 50.58 Y. Mizoshita, S. Hasegawa, K. Takaishi: Vibration minimized access control for disk drive, *IEEE Trans. Magn.* **32**, 1793–1798 (1996)
- 50.59 P. Vettiger, G. Cross, M. Despont, U. Drechsler, U. Durig, B. Gotsmann, W. Haberle, M. A. Lantz, H. W. Rothuizen, R. Stutz, G. K. Binnig: The “millipede”—nanotechnology entering data storage, *IEEE Trans. Nanotechnol.* **1**, 39–55 (2002)
- 50.60 <sup>TS21</sup> D. Hernandez, S.-S. Park, R. Horowitz, A. K. Packard: Dual-stage track-following servo design for hard disk drives, Proc. of American Automatic Control Conference, ed. by <sup>TS19</sup> (IEEE, Piscataway 1999) 4116–4121
- 50.61 <sup>TS21</sup> M. Rotunno, R. A. de Callafon: Fixed order  $H_\infty$  control design for dual-stage hard disk drives, Proc. of the 39th IEEE Conference on Decision and Control, ed. by <sup>TS19</sup> (IEEE, Piscataway 2000) 3118–3119
- 50.62 <sup>TS21</sup> K. J. Åström, B. Wittenmark: *Adaptive Control*, 2nd edn. (Addison-Wesley, Reading 1995)
- 50.63 <sup>TS21</sup> M. T. White, W.-M. Lu: Hard disk drive bandwidth limitations due to sampling frequency and computational delay, Proc. of the 1999 IEEE/ASME International Conference on Intelligent Mechatronics, ed. by <sup>TS19</sup> (IEEE, Piscataway 1999) 120–125
- 50.64 <sup>TS21</sup> Y. Li, R. Horowitz: Design and testing of track-following controllers for dual-stage servo systems with PZT actuated suspensions [in HDD], *Microsyst. Technol.* **8**, 194–205 (2002)

<sup>CE20</sup> Note: Publisher location omitted<sup>TS21</sup> This reference is not cited in the text.

